

THE SIZES OF DIFFUSE LY α NEBULAE AROUND STAR-FORMING GALAXIES AT HIGH REDSHIFT

RUI XUE,¹ KYOUNG-SOO LEE,^{1,*} ARJUN DEY,² NAVEEN REDDY,^{3,†} SUNGRYONG HONG,⁴ MOIRE K. M. PRESCOTT,⁵
HANAE INAMI,⁶ BUELL T. JANNUZI,⁶ AND ANTHONY H. GONZALEZ⁷

¹*Department of Physics and Astronomy, Purdue University, 525 Northwestern Avenue, West Lafayette, IN 47907*

²*National Optical Astronomy Observatory, 950 N. Cherry Avenue, Tucson, AZ 85719*

³*Department of Physics and Astronomy, University of California, Riverside, 900 University Avenue, Riverside, CA 92521*

⁴*Department of Astronomy, University of Texas at Austin, 2515 Speedway, Stop C1400, Austin, TX 78712*

⁵*Department of Astronomy, New Mexico State University, PO Box 30001, Las Cruces, NM 88001*

⁶*Steward Observatory, University of Arizona, 933 N Cherry Ave, Tucson, AZ 85721*

⁷*Department of Astronomy, University of Florida, 211 Bryant Space Science Center, Gainesville, FL 32611*

ABSTRACT

We report the detection of diffuse Ly α emission, or Lyman alpha halos (LAHs), around star-forming galaxies at $z \approx 3.78$ and 2.66 in the NOAO Deep Wide-Field Survey Boötes field. Our samples consist of a total of $\approx 1,400$ galaxies, within two separate regions containing spectroscopically confirmed galaxy overdensities. They provide a unique opportunity to investigate how the LAH characteristics vary with host galaxy large-scale environment and physical properties. We stack Ly α images of different samples defined by these properties and measure their median LAH sizes by decomposing the stacked Ly α radial profile into a compact galaxy-like and an extended halo-like component. We find that the exponential scalelength of LAHs depends on UV continuum and Ly α luminosities, but not on Ly α equivalent widths or galaxy overdensity parameters. The full samples, which are dominated by low UV-continuum luminosity Ly α emitters ($M_{UV} \gtrsim -21$), exhibit LAH sizes of 5–6 kpc. However, the most UV luminous galaxies have more extended halos with scalelengths of 8–9 kpc. The stacked Ly α radial profiles of our samples decline more steeply than recent theoretical predictions that include the contributions from gravitational cooling of infalling gas and from low-level star formation in satellites. However, the LAH extent and surface brightness profile matches what one would expect for photons produced in the galaxy and then resonantly scattered by gas in an outflowing envelope. The observed trends of LAH sizes with host galaxy properties suggest that the physical conditions of the CGM (covering fraction, HI column density, and outflow velocity) change with halo mass and/or star formation rates.

Keywords: cosmology:observations – galaxies:clusters – galaxies:distances and redshifts – galaxies:evolution – galaxies:formation – galaxies:high-redshift

* Visiting Astronomer, Kitt Peak National Observatory, National Optical Astronomy Observatory, which is operated by the Association of Universities for Research in Astronomy (AURA) under cooperative agreement with the National Science Foundation.

† Sloan Research Fellow

1. INTRODUCTION

The circumgalactic medium (CGM) encodes the details of two main physical processes that shape how galaxies form and evolve: namely, the gas accretion that fuels star formation; and the resulting feedback. Constraining the spatial distribution and dynamical state of the CGM around high-redshift galaxies is thus of critical importance to test our current theoretical framework of galaxy formation.

However, the diffuse nature of the CGM poses a major observational challenge. Direct 21 cm imaging of atomic gas in the CGM is beyond the capability of current instruments (Carilli & Rawlings 2004). While absorption sightlines can probe the CGM (e.g. Steidel et al. 2010; Tumlinson et al. 2013), inferring the gas distribution from them is nontrivial due to the discrete sampling of bright background sources. Diffuse Ly α emission, or Lyman alpha halos (LAHs), around high-redshift galaxies, may open a new avenue for the CGM study: Ly α photons – which are presumably produced copiously at sites of star formation – can be resonantly scattered by neutral hydrogen gas out to large galactocentric distances; as a result, the Ly α emission is expected to appear more extended than the rest-frame UV continuum. With sophisticated and self-consistent models of Ly α radiative transfer modeling, it is possible to follow how Ly α photons propagate through simulated interstellar, circumgalactic, and intergalactic media. Comparisons between models and observations may provide invaluable insight into the physical properties of the CGM neutral gas (Zheng et al. 2011; Verhamme et al. 2012; Dijkstra & Kramer 2012; Lake et al. 2015).

At high redshift, there is growing evidence for the presence of LAHs around high-redshift star-forming galaxies (Hayashino et al. 2004; Rauch et al. 2008; Steidel et al. 2011; Matsuda et al. 2012; Momose et al. 2014, 2016), although a few studies find only marginal evidence in their samples (e.g., Feldmeier et al. 2013; Jiang et al. 2013). Recent Ly α and UV observations also suggest that Ly α emitting galaxies in the local universe ubiquitously produce large-scale halos of scattered Ly α emission (Hayes 2015). In spite of the observational progress, it is still unclear what is the dominant power source that produces extended Ly α emission around galaxies. While star formation inside the host galaxy is likely to produce Ly α photons that scatter through the medium, spatially extended Ly α emission may also originate from widespread low-level star formation activity or from the cooling radiation of collisionally heated infalling gas, beyond the regions revealed by rest-frame UV or IR emission. The uncertainty of ionizing source distributions from these auxiliary mechanisms remains a major obstacle to establishing a direct relation between the appearance of LAHs and the physical properties of CGM.

On the other hand, the variations of LAH characteristics measured in different high-redshift galaxy samples clearly require physical explanations. Based on different sample selections, some studies find more extended halos (Steidel et al. 2011, hereafter S11) than others (Feldmeier et al. 2013; Momose et al. 2014; Wisotzki et al. 2016). The difference could be elaborated by considering various scenarios: the spatial and velocity structures of the ISM and CGM likely change as a function of galaxy properties and host halo (e.g., Jones et al. 2013; Williams et al. 2015), which can alter Ly α photon propagation and the LAH surface brightness profile; the Ly α spatial extent may be also strongly related to the surrounding Mpc-scale environments (Matsuda et al. 2012), provided that the CGM gas structure or the ionizing source distribution outside the host galaxy (i.e., satellite galaxies and gas accretion) is related to the dark matter distribution (e.g., Laursen & Sommer-Larsen 2007; Zheng et al. 2011). Identification of a clear trend of how LAH characteristics depend on other galaxy properties may provide a promising avenue to elucidate the origin of the LAH phenomenon and its connection with the CGM.

In this paper, we present new LAH measurements based on two of the largest spectroscopic and photometric samples of high-redshift star-forming galaxies. We focus on how LAH characteristics change with galaxy UV continuum and Ly α luminosities, and large scale environment. This is achieved in practice by stacking Ly α and UV continuum images of subsets of galaxies binned by a specific property. The paper is organized as follows. In §2, we describe the datasets, sample selection, and other notable facts about our survey fields. In §3, we present the methodology adopted for the image stacking analysis and measurements of the LAH properties. In §4 is discussed the characterization of galaxies' large scale environment, one of the key parameters we explore in the LAH size dependence. Our main findings are described in §5. In §6, we discuss the implications of our results in the context of recent theoretical predictions. Finally, the summary of our results and conclusions are given in §7.

Throughout this paper, we use the WMAP7 cosmology ($\Omega, \Omega_\Lambda, \sigma_8, h$) = (0.27, 0.73, 0.8, 0.7) from Komatsu et al. (2011). Distance scales are presented in units of comoving Mpc unless noted otherwise. All magnitudes are given in the AB system (Oke & Gunn 1983).

2. DATA AND SAMPLES OF GALAXIES IN DIVERSE ENVIRONMENTS

We consider two galaxy samples for our investigation. These samples consist of star-forming galaxies at $z \approx 3.78$ and 2.66, and populate two non-overlapping regions in the Boötes field of the NOAO Deep Wide-Field Survey (NDWFS; Jannuzi & Dey 1999). Here, we briefly describe the samples and their characteristics.

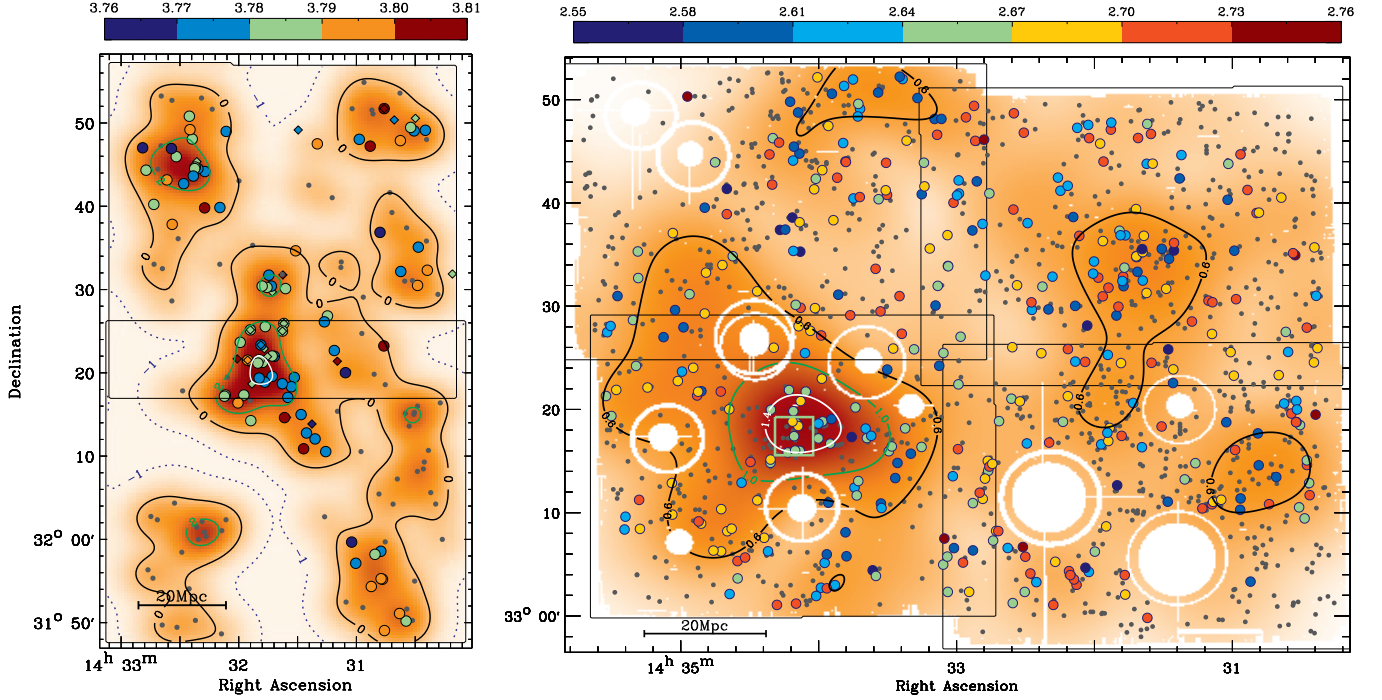


Figure 1. *Left:* the surface overdensity map of the LAEs detected at $z \approx 3.78$ in the PCF field, shown in color scale and contours. The positions of photometric LAEs are in gray dots, while spectroscopic sources are color coded in redshift (filled circles and diamonds for LAEs and LBGs, respectively). The coverages of the PCF-N and -S pointings are indicated by solid black boxes. As described in §4.1, the overdensity map is derived from the LAE surface density, which is constructed by smoothing the LAE positions with a 2D Gaussian kernel of FWHM = $4.8'$, or 10 Mpc at $z = 3.78$. *Right:* the second moment map of the 3D overdensity of the spectroscopic LAEs in the LAB field at $z \approx 2.66$, shown in color scale. Gray dots represent the photometric LAEs, while the positions of spectroscopically confirmed LAEs at $z = 2.569 - 2.737$ are indicated by filled circles, color coded with redshift as indicated by the color bar on top. The boundaries of four LAB pointings are marked with solid black boxes, and the masked regions (due to image saturation and other artifacts) are in white. The 3D overdensity of the LAB field is derived from the number density of the spectroscopic LAEs, which is estimated by smoothing their distribution with a 3D Gaussian kernel of FWHM = 20 Mpc at $z = 2.66$. The comoving distance scale at corresponding sample redshift is indicated at the bottom left corner of each panel.

2.1. Galaxies around PC 217.96+32.3 at $z \approx 3.78$

The first sample consists of galaxies at $z \approx 3.78$, and will be referred to as the “PCF” (protocluster field) sample hereafter. These galaxies are distributed over a $1.2^\circ \times 0.6^\circ$ contiguous region located at the southern edge of the Boötes field (center: $\alpha = 217.86^\circ$, $\delta = 32.33^\circ$). The optical imaging data are taken with the Mosaic 1.1 wide-field imaging camera on the Mayall 4m telescope of the Kitt Peak National Observatory. The field consists of two adjacent pointings with a $9'$ overlap in the north-south direction (see Figure 1). The northern pointing (PCF-N) coincides with an NDWFS subfield named NDWFSJ1431+3236, while the southern pointing (PCF-S) lies outside the NDWFS boundary. The PCF-N imaging includes the NDWFS data¹, complemented by our new observations taken in May

2012. The PCF-S observations are taken in May and June 2014, closely matching the sensitivities of the PCF-N data. The entire PCF field is observed with four NOAO filters: three broad-band filters (B_W , R , I ; $\lambda_{\text{cen}} = 4222, 6652, 8118\text{\AA}$) and one narrow-band filter WRC_4 . The WRC_4 filter is designed to sample C IV emission in Wolf-Rayet stars (KPNO filter no. k1024). In the KPNO 4m f/3.1 prime-focus corrector beam, it has a central wavelength of 5819\AA and a FWHM of 42\AA , which can sample Ly α emission at $3.775 < z < 3.810$ (i.e., 27 comoving Mpc along the line of sight). At the same redshift, the three broadband central wavelengths correspond to rest-frame wavelengths of 882, 1390, and 1697\AA , respectively. The details of these observations are presented in Lee et al. (2014) and Dey et al. (2016).

The galaxies in the PCF sample are selected as Lyman alpha emitters (LAEs) or Lyman break galaxies (LBGs). The LAE selection requires blue narrowband-to-broadband colors ($WRC_4 - R$), which is designed to isolate galaxies that have an excess Ly α emission

¹ <http://www.noao.edu/noao/noaodeep/DR3/dr3-data.html>

in the *WRC4* band. The LBG candidates are selected by applying a Lyman break color selection technique to the *B_WRI* data (e.g., [Steidel et al. 1999](#); [Giavalisco et al. 2004](#); [Bouwens et al. 2007](#); [Lee et al. 2011](#)). The technique is designed to identify UV-bright star-forming galaxies at $3.3 < z < 4.3$, that show strong Lyman break at rest-frame $\lambda \leq 1216\text{\AA}$ (between the *B_W* and *R* bands). The adopted LAE color criteria are:

$$(WRC4 - R) < -0.8 \quad \cap \quad S/N(WRC4) \geq 7 \\ \cap [(B_W - R) > 1.8 \quad \cup \quad S/N(B_W) < 2], \quad (1)$$

and the LBG color criteria are:

$$(B_W - R) > 3(R - I) + 1.74 \quad \cap \quad (B_W - R) \geq 1.8 \\ (R - I) \geq -0.54 \quad \cap \quad S/N(R) \geq 3 \quad \cap \quad S/N(I) \geq 7. \quad (2)$$

Followup spectroscopy was carried out targeting a subset of the photometric LBG and LAE samples, the results of which are described in [Lee et al. \(2013\)](#) and [Dey et al. \(2016\)](#). Briefly, of the 165 LAE candidates, 100 are observed and only two of which are identified as [O II] emitters at low redshift. Counting null detections and two interlopers as failures, the spectroscopic success rate for LAEs is found to be 89%, suggesting that the majority of unobserved LAEs also lie at the expected redshift range, $z \approx 3.78$. None of the confirmed LAEs show evidence of strong AGN activity in their spectra (i.e., broad/strong lines of high ionization species). Hence, we include the entire photometric sample of LAEs (excluding the two confirmed interlopers) for our analyses. On the other hand, the LBG candidates span a much wider redshift range ($z = 3.7 \pm 0.4$, [Lee et al. 2013](#)), and therefore we only include LBGs that are spectroscopically confirmed to lie at the same range as LAEs: $z_{\text{spec}} = 3.775\text{--}3.810$. Table 1 includes the numbers of LAEs and LBGs in the PCF field used for the present analyses.

Within the PCF field lie two massive protoclusters at $z = 3.78$, which we collectively dub PC 217.96+32.3. One is located near the field center at $(\alpha, \delta) = (217.91^\circ, +32.35^\circ)$ and contains 39 spectroscopically confirmed members at $z = 3.774\text{--}3.790$, while the other is located at the northeastern corner of the field, $(\alpha, \delta) = (218.15^\circ, +32.75^\circ)$, with 16 confirmed members at $z = 3.775\text{--}3.796$. [Dey et al. \(2016\)](#) estimated the total masses enclosed to be $\approx 10^{15}M_\odot$, and $\approx 6 \times 10^{14}M_\odot$ for the central and northeastern structures, respectively. Both structures represent extremely rare high-overdensity regions, and are expected to evolve into massive galaxy clusters by the present-day epoch. Further discussion on the environment measurements in and around these structures is given in § 4.

2.2. Galaxies around LABd05 at $z \approx 2.66$

Our second sample consists of LAEs around a giant Ly α nebula or Lyman alpha blob (LAB) at $z = 2.656$

within the Boötes field at $(\alpha, \delta) = (218.546^\circ, 33.291^\circ)$. The nebula, known as LABd05, has a line luminosity $L_{\text{Ly}\alpha} \approx 1.7 \times 10^{44} \text{ erg s}^{-1}$, and is spatially extended to a radius of at least $15''$ or $\approx 120 \text{ kpc}$ ([Dey et al. 2005](#)). The optical dataset includes the broadband NDWFS *B_WRI* data and the *IA445* intermediate-band filter data ($\lambda_{\text{cen}} = 4458, \Delta\lambda = 201$) taken with the SuprimeCam imager on the Subaru telescope. The *IA445* filter can sample the redshifted Ly α emission at $z = 2.569\text{--}2.737$, corresponding to the line-of-sight comoving distance of $\approx 190 \text{ Mpc}$. Four adjacent pointings are taken in each filter, covering a 1 deg^2 contiguous region (see Figure 1).

The adopted LAE selection criteria are:

$$(IA445 - B_W) < -0.5 \quad \cap \quad S/N(IA445) > 7 \\ \cap \quad B_W - R \leq 0.8. \quad (3)$$

The first criterion isolates galaxies with a strong emission line falling into the *IA445* band, while the last one is intended to eliminate contaminant populations, namely [O II] emitters at $z \approx 0.2$ or higher-redshift star-forming galaxies at $z \gtrsim 3$. More details of the Subaru observation, data reduction, and candidate selection are provided in [Prescott et al. \(2008\)](#). The selection yields 1,336 LAE photometric candidates. The LAE candidates in this field, which we refer to as the LAB sample, are expected to have the rest-frame equivalent widths of $EW_0 \gtrsim 50\text{\AA}$, and thus are typically stronger line emitters than the LAEs in the PCF field ($\geq 20\text{\AA}$).

Followup spectroscopy was performed on a subset of LAEs with the Hectospec instrument, a bench-mounted fiber spectrograph on the 6.5m MMT. The Hectospec observation consisted of 7 pointings whose center positions are offset up to $30'$ from one another in the RA direction to cover the entire field. While the details of target selection and spectroscopic observations are presented in [Hong et al. \(2014\)](#), one notable fact is that the angular distribution of spectroscopic sources is not uniform across the field due to the technical limitations of assigning fibers to sources far from pointing center. As a result, the middle two-thirds of the LAB field is more densely populated by spectroscopic LAEs than the eastern and western end of the LAB field.

The observations confirmed 429 LAEs at $z = 2.569\text{--}2.737$, corresponding to $\approx 87\%$ of the LAE candidates with spectroscopic redshifts, suggesting a relatively clean photometric selection for our LAE sample. The imaging field of the LAB sample also contains at least one overdensity region. In the immediate vicinity of LABd05 lie multiple companions, including an AGN and an LBG within the nebula ([Dey et al. 2005](#)). Deep *HST* imaging revealed a population of compact low-luminosity galaxies in its vicinity, and [Prescott et al. \(2012\)](#) argued this as evidence that LABd05 is a site of an ongoing group formation. Their speculation is corroborated by the MMT spectroscopy which identified 168 LAEs within $\Delta z = \pm 0.02$ of the LABd05. In § 4,

we further quantify the LAE-defined local environments within the PCF and LAB fields.

3. TESTING FOR THE PRESENCE OF DIFFUSE EMISSION AROUND GALAXIES

Our primary goal is to test for the presence of LAHs around galaxies in our samples. Because the $\text{Ly}\alpha$ sensitivity of our observations is lower than the expected surface brightness of an LAH, we determine average light profiles by stacking the images of many galaxies. In practice, this is a challenging task because diffuse emission can be easily mimicked by observational factors, such as image mis-registration, point spread functions, or imperfect sky subtraction that varies from field to field. Some of these effects are discussed extensively in [Feldmeier et al. \(2013\)](#). In this section, we describe the procedures for our image analyses and various tests we performed to quantify uncertainties.

3.1. Image Registration, PSF, and PSF Matching

Two critical elements for robust stacking analyses are image registration and point spread function (PSF) homogenization among all imaging data. Both misregistration and varying PSFs can artificially broaden the average light profile. We eliminate these possibilities by employing the procedures described below.

For each exposure of a given pointing, we update the astrometry (employing the `iraf`² task `mscresd` `msccmatch`) using stars identified in the Sloan Digital Sky Survey DR7 Catalog, and reproject it to a common tangent point using a sinc interpolator with a pixel scale of $0.258'' \text{ pixel}^{-1}$. The same procedure is repeated for all available frames from new observations or the NDWFS archive. The typical RMS in the astrometric solution is $0.05'' - 0.08''$. For each pointing per band, a final mosaicked image is created as a weighted average of all frames, with weights inversely proportional to the variance of sky noise measured in the reprojected individual frames.

Next, we determine the PSFs of individual images using two different approaches. In the first method, we adopt a procedure similar to that outlined by [Feldmeier et al. \(2013\)](#) as follows. We first run SEXTRACTOR ([Bertin & Arnouts 1996](#)) to create the source catalog of each image. A list of relatively bright but unsaturated stars is created based on the compactness parameter (`CLASS_STAR` > 0.95), and then cross-referenced with the Guide Star Catalogs v2.3.2 (GSC, `CLASS` = 0; [Lasker et al. 2008](#)). Based on the catalogs and visual inspection, sources with blending issues or with a companion within $5''$ are removed from the list. We measure the radial profile of each star by azimuthally averaging in bins

of annuli, and normalize the profile at $2''$ from center. Then we take a median average of all normalized star radial profiles to derive the PSFs out to $4''$. Independently from this procedure, we measure the large-scale ‘wings’ of the PSF from the GSC stars that are saturated in our data. We first mask saturated pixels and determine the centroids by fitting a two-dimensional Gaussian function to the unmasked pixels. The outer radial profile is then measured at $2'' - 6''$, and is combined with the inner profile by matching the amplitude at $3''$.

In an alternative approach, we use a software PSFEX ([Bertin 2011](#)) to derive PSF models. PSFEX uses the information supplied by a SEXTRACTOR source catalog to iteratively reject sources that are saturated, contaminated, or extended, and then automatically selects point source candidates to construct a non-parametric PSF model. Specifically, for each image, we supply a input catalog including the sources with `ELLIPTICITY` < 0.1 and `SNR_WIN` > 30 , where `ELLIPTICITY` and `SNR_WIN` are SExtractor parameters defined as source ellipticity and window-based signal-to-noise ratio, respectively. Although PSFEX will reject any saturated sources and does not use the broad light profile of saturated objects to derive PSF as our first method, a larger number of point sources are usually included to construct the PSF due to the efficient automated selection criteria. In the PSFEX-based method, we also model the PSF spatial variation within each image using second-order polynomial components. However, a zeroth order polynomial component is found to adequately describe all PSFs (see details below) and therefore adopted for our analyses.

In the left panels of Figure 2, we compare the stellar PSFs determined by the GSC-based (histograms) and PSFEX-based (open symbols) methods, with colors representing different pointings and passbands. The results clearly illustrate large PSF differences within our datasets, but two methods are evidently in excellent agreement with one another for a given image. For simplicity, we adopt the PSFEX-based PSF models for all image analyses in this study. The PSF FWHM of each image is listed in Table 2.

We homogenize the PSFs by convolving all images in each field to the reference PSF which is taken as that of the worst seeing data in the dataset. For example, the reference PSF for the PCF sample is from the *I*-band image of the PCF-S pointing (see Table 2). A smooth convolution kernel is derived by comparing the circularized PSF³ of each image with the reference using an IDL deconvolution routine `MAX_LIKELIHOOD`. The kernel is then used to convolve the image using the IDL `CONVOL` routine. We repeat the PSFEX-based measurement pro-

² IRAF is distributed by the National Optical Astronomy Observatory, which is operated by the Association of Universities for Research in Astronomy (AURA) under cooperative agreement with the National Science Foundation.

³ A circularized PSF is generated from the radially medium-averaged PSF image produced by PSFEX, leading to a higher SNR at the outer profile at the expense of simplifying the PSF into a 1D function. Using circularized PSF for deriving kernels will produce a convolution kernel which is noiseless.

Table 1. Sample Summary and Comparisons with Literature

Field	Selection	Sample Size ^a	Redshift ^b	δ kernel ^c	Reference
PCF	LAE	163	3.775 – 3.810	Gaussian	This Work
-	LBG	21	3.775 – 3.810	$\sigma = 2.0' (4.3 \text{ Mpc})$	"
LAB	LAE	1336	2.569 – 2.737	$\sigma = 4.8' (8.6 \text{ Mpc})$	"
HS1549+195	LBG	27	2.802 – 2.875	...	Steidel et al. (2011)
HS1700+643	LBG	43	2.266 – 2.340	...	"
SSA22a	LBG	22	3.063 – 3.129	...	"
GOODS-N+SDF+	LAE	2128	3.062 – 3.126	Gaussian	Matsuda et al. (2012)
SXDS+extended SSA22a	LBG	24	3.062 – 3.126	$\sigma = 1.5' (2.9 \text{ Mpc})$	
SXDS	LAE	316	3.106 – 3.167	...	Momose et al. (2014)
-	LAE	100	3.663 – 3.720	...	"
-	LAE	397	5.655 – 5.753	...	"
-	LAE	119	6.510 – 6.619	...	"
COSMOS+GOODS	LAE	3556	2.145 – 2.222	Tophat	Momose et al. (2016)
+SSA22+SXDS				$r = 10' (16.2 \text{ Mpc})$	"

^a The sizes of our samples here represent the number of galaxies selected for image stacking. For the PCF and LAB samples, 98 and 429 galaxies have been confirmed spectroscopically within the expected redshift ranges, respectively.

^b The photometric redshift range is derived by filter half-power points.

^c The smoothing kernel used to derive overdensity (FWHM in parentheses).

Table 2. Imaging Data and PSF Summary

Dataset/ Redshift	Pointing Name ^a	<i>WRC4</i> 5820Å/42Å ^b	<i>IA445</i> 4458Å/201Å	<i>B_W</i> 4222Å/1275Å	<i>R</i> 6652Å/1511Å	<i>I</i> 8118Å/1915Å
PCF/ $z \approx 3.78$	PCF-N (J1431p3236)	0.88''	...	(0.97'')	0.95''	0.77''
	PCF-S	1.00''	...	(1.28'')	0.97''	<u>1.10''</u>
	NDWFS1 (J1434p3311)	...	0.73''	1.00''	1.17''	(0.95'')
LAB/ $z \approx 2.66$	NDWFS4 (J1431p3311)	...	0.80''	1.13''	1.05''	(1.10'')
	NDWFS5 (J1434p3346)	...	0.95''	0.97''	0.85''	(1.14'')
	NDWFS6 (J1431p3346)	...	1.00''	<u>1.37''</u>	1.14''	(1.00'')

^a The corresponding NDWFS subfield names (from DR2) are given in parentheses, with the prefix ‘NDWFS’ omitted

^b The filter central wavelength/FWHM, $\lambda_{\text{cen}}/\Delta\lambda$

NOTE— The PSF sizes (FWHMs) are measured from the PSFEX models (see descriptions in §3.1). We use parentheses to denote the archival NDWFs data that are not included in our image analyses. The underlined values correspond to the worst seeing data in individual used datasets.

cedure on the PSF-homogenized images using the same set of stars. The results are presented in the middle panels of Figure 2, showing that the PSFs within a given dataset are now in reasonable agreement with one another out to 6'' for the stacking purpose. The FWHMs of homogenized PSFs are 1.10'' and 1.37'' for the PCF and LAB sample, respectively. In the right panels of Figure 2, we present the estimated PSF spatial variation in

the PSF-homogenized NB images. Because the variations are mild as illustrated, adopting spatially varying PSFs for our subsequent analyses will have little impact on our main conclusions.

3.2. Measuring Light Profiles of Galaxies

Having homogenized all the images to a common PSF within $\approx 6''$, we adopt the following procedure for image

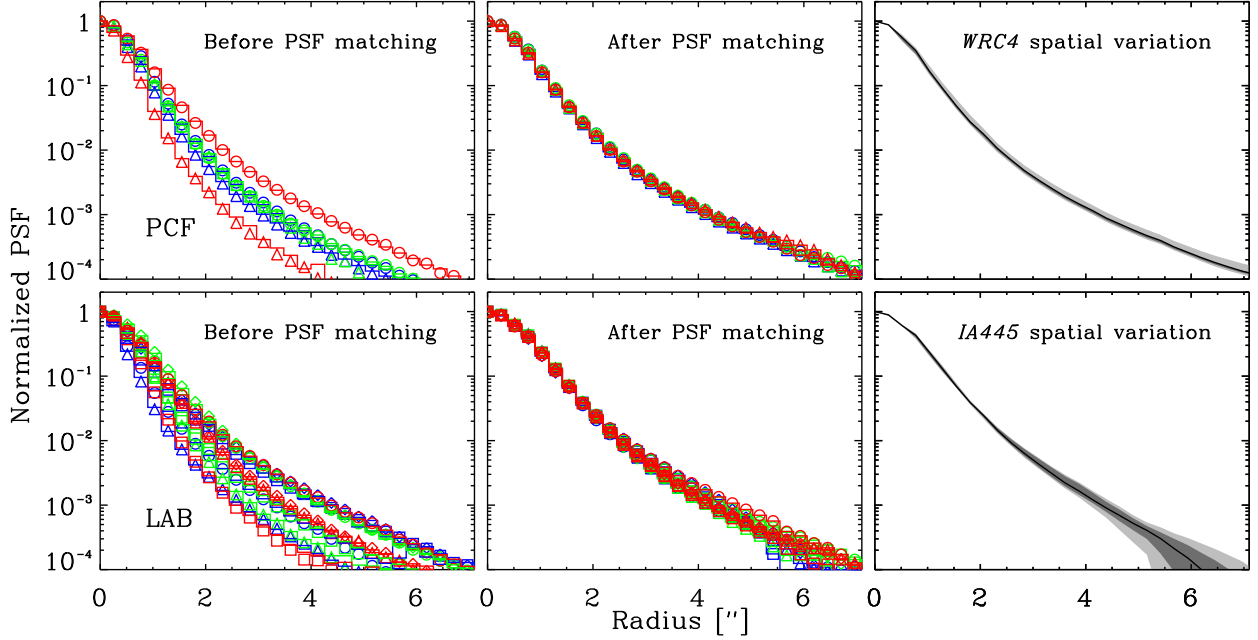


Figure 2. The radially averaged light profiles of Galactic stars are measured to determine the point spread functions of the PCF (top) and LAB (bottom) image tiles. The left panels show the PSF measurements of original images. The colors of lines and symbols represent different combinations of pointings and passbands. As described in §3.1, two different methods are employed to determine the PSFs, which are shown as color histograms (GSC-based) and symbols (PSFEx-based) in each panel. Both methods return very similar results, and allows us to robustly characterize the PSF effects on observed light profiles of galaxies within a dynamic range of up to ~ 3 – 4 orders of magnitude. In the middle panels, we show the PSF measurements of all image tiles after PSF homogenization, suggesting that they are in good agreement out to $\approx 6''$. We evaluate the PSF spatial variations within each image using PSFEx. In the right panels, we present 10–90% and 25–75% range of estimated position-dependent PSF at sample galaxies locations as the light and dark gray shades, derived from PSF-homogenized NB images. The black lines show the median profiles.

stacking preparation and galaxy light profile measurements:

First, we make a $1' \times 1'$ cutout image centered on each galaxy. SEXTRACTOR is run on the image twice to detect all objects down to 1.5σ and 2σ with DETECT_MINAREA = 5 pixel and BACK_SIZE = $30''$. We apply a Gaussian filter with a FWHM of 2 pixels for improving detection of extended faint objects. Using the SEXTRACTOR segmentation maps, we mask all 2σ detection pixels belonging to interlopers (i.e., sources not at center) and expand individual mask regions to adjacent 1.5σ regions for a more robust exclusion of low-level contaminants. Cutout images are then over-sampled to $0.086''/\text{pixel}$ (i.e., one third of the original pixel size) using a nearest-neighbor interpolation, with the object centroid located at the center pixel of the resampled image. Finer resampling ensures that image stacking can be conducted without introducing further broadening due to sub-pixel centroid uncertainties. Finally, we “repair” the masked regions as follows. For each pixel within mask regions, we determine its distance from the galaxy center. Then we replace its value with the median value of the unmasked pixels at a similar projected galactocentric distance and further add

pseudo noise commensurate with the measured cutout background noise. This additional step ensures all objects contribute equally to each pixel of the stacked image. Generally, less than 20% of the pixels in the cutout images are masked. Whenever more than 20% of the area is masked out, we do not include the galaxy in stacking procedure.

Following the method detailed in Appendix A, we create $\text{Ly}\alpha$ and line-free continuum images at rest-frame $\approx 1220\text{\AA}$ using two bands sampling both $\text{Ly}\alpha$ and UV continuum emission, which we refer to as the narrow and broad bands⁴ (NB and BB). The median 3σ surface brightness sensitivity of individual resampled cutout $\text{Ly}\alpha$ images are 6.3×10^{-18} and $13.2 \times 10^{-18} \text{ erg s}^{-1} \text{ cm}^{-2} \text{ arcsec}^{-2}$ in the PCF and LAB sample, respectively. For the galaxies at $z \approx 3.78$ or $z \approx 2.66$, we use the I or R band images to estimate their UV continuum at rest-frame $\approx 1700\text{\AA}$ (referred as the continuum band, or CB). The median 3σ surface bright-

⁴ The referred NB and BB are *WRC4* and *R* bands for the PCF sample, and *IA445* and *B_W* bands for the LAB sample, respectively. Although *IA445* is an intermediate band filter, we prefer it as NB here for notational convenience.

ness sensitivities of cutout images reach 9.5×10^{-31} and $7.2 \times 10^{-31} \text{ erg s}^{-1} \text{ cm}^{-2} \text{ arcsec}^{-2} \text{ Hz}^{-1}$, respectively.

To create a stacked image for a given galaxy sample, we exclude the galaxies that are within $5''$ from a bright source, within $1'$ from the edges of the science image, or of the masked regions near bright saturated stars (shown in Figure 1), then simply take a pixel-to-pixel median of the resampled, re-centered cutout images. This procedure excludes $\approx 13\%$ and $\approx 2\%$ of the LAB sample and PCF sample, respectively. The higher level of source removal in the LAB sample is a result of the fact that the Subaru *IA445* band image contains a larger number of artifacts (CCD bleeding and diffraction spikes around bright stars; see Figure 1), thus requires more aggressive masking in order to avoid contamination.

The cutout images likely still contain emission from nearby sources below our adopted detection threshold. They may introduce negative or positive bias regions in Ly α cutout images due to imperfect continuum subtraction. However, assuming that these undetected objects are randomly distributed in individual cutout images without the presence of clustering, their contribution should be similar across all pixels of the stacked image. To create a “contamination-free” stacked image, we estimate the effective background using an annular region from $6''$ to $10''$ and subtract its median value from the stacked image. This procedure removes the bias introduced by undetected objects, but limits our ability to detect any diffuse emission beyond the central region $12''$ in diameter (corresponding to 88 kpc and 98 kpc in the angular distance, for our samples at $z = 3.78$ and $z = 2.66$, respectively). The choice of the annular region size will be further discussed in Appendix B.

The radial surface brightness profiles are measured by azimuthally averaging the pixel values in successive bins of annuli from source center. We find that the median and mean averaging within the annuli give consistent results in all cases of our study. Here, we adopt median averaging results as observed light profiles. To characterize the spatial extent of Ly α emission, we fit the radial profile using two different models:

In the first model, we assume the Ly α surface brightness as an exponentially declining function of projected galactocentric distance,

$$S(r) = S_0 \exp(-r/r_s), \quad (4)$$

where r_s is the exponential scalelength, and S_0 is the surface brightness at source center. This simple approach was adopted in several previous works (Steidel et al. 2011; Matsuda et al. 2012; Feldmeier et al. 2013; Momose et al. 2014), with the caveat that the center light profile could be heavily influenced by the PSF. The measurements may also suffer from large uncertainties at large radii where the surface brightness profile is lost in the background noise. In our analysis, we only fit the radial profile in the range $r = [1.75'', 6.00'']$, similar to other analyses in the literature. The range corresponds

to 13–44 kpc for the PCF sample, or 14–49 kpc for the LAB sample.

The second model is motivated by Wisotzki et al. (2016), in which a Ly α radial profile is fit with two separate model components convolved with the image PSF: a core ‘galaxy’ component with a compact exponential profile and a separate broader halo component which also declines exponentially. The two-component model can be parametrized as:

$$S(r) = \text{PSF} * [S_c \exp(-r/r_{s,c}) + S_h \exp(-r/r_{s,h})] \quad (5)$$

$$I(r) = \text{PSF} * I_c \exp(-r/r_{s,c}) \quad (6)$$

where the exponential scales of two components are $r_{s,h}$ and $r_{s,c}$ (“c” and “h” denote the continuum and halo component, respectively). $S(r)$ and $I(r)$ present the Ly α and UV surface brightness, respectively. We simultaneously fit both of the Ly α and UV continuum using the above model, with $r_{s,c}$ largely constrained by the continuum light profile. This decomposition model automatically accounts for the PSF effect on both Ly α and UV continuum images, such that we can take a full advantage of the measured radial profile at all ranges. On the other hand, the uncertainties of the single-component scalelength is expected to be more sensitive to the selected projected galactocentric radii and large-scale PSF profile. We refer interested readers to Appendix C, where we provide extensive discussions on this topic.

3.3. Definitive Detection of Diffuse Ly α Emission around Galaxies

In Figures 3 and 4, we present the stacked galaxy images and their corresponding one-dimensional surface brightness radial profiles, which are constructed from the full LAE samples in the LAB and PCF fields at $z \approx 2.66$ and $z \approx 3.78$, respectively. The emission in the Ly α or NB filters is clearly more extended than that in the continuum bands or stellar PSFs, while the BB image stacks (*I* and *R*-band for the PCF and LAB sample, respectively) are consistent with their respective stellar PSFs. We further test the validity of our detection by repeating the stacking procedure on a sample of randomly selected NB-detected sources within the same brightness range. The radial profiles of these control samples are consistent with stellar PSFs in *all* bands, eliminating the possibility that the extended emission is originating from the passband-dependent large-scale PSF wings (Feldmeier et al. 2013) or artifacts of our stacking procedures.

In Tables 3 and 4, we list the LAH scalelengths estimated from both profile fitting methods, with their uncertainties evaluated at 90% confidence level. These uncertainty limits are estimated using Monte Carlo simulations by repeatedly fitting models to new realizations of stacking light profiles with added systematic and statistical noise. For both PCF ($z = 3.78$) and LAB ($z = 2.66$) samples, we measure the Ly α scalelengths r_s

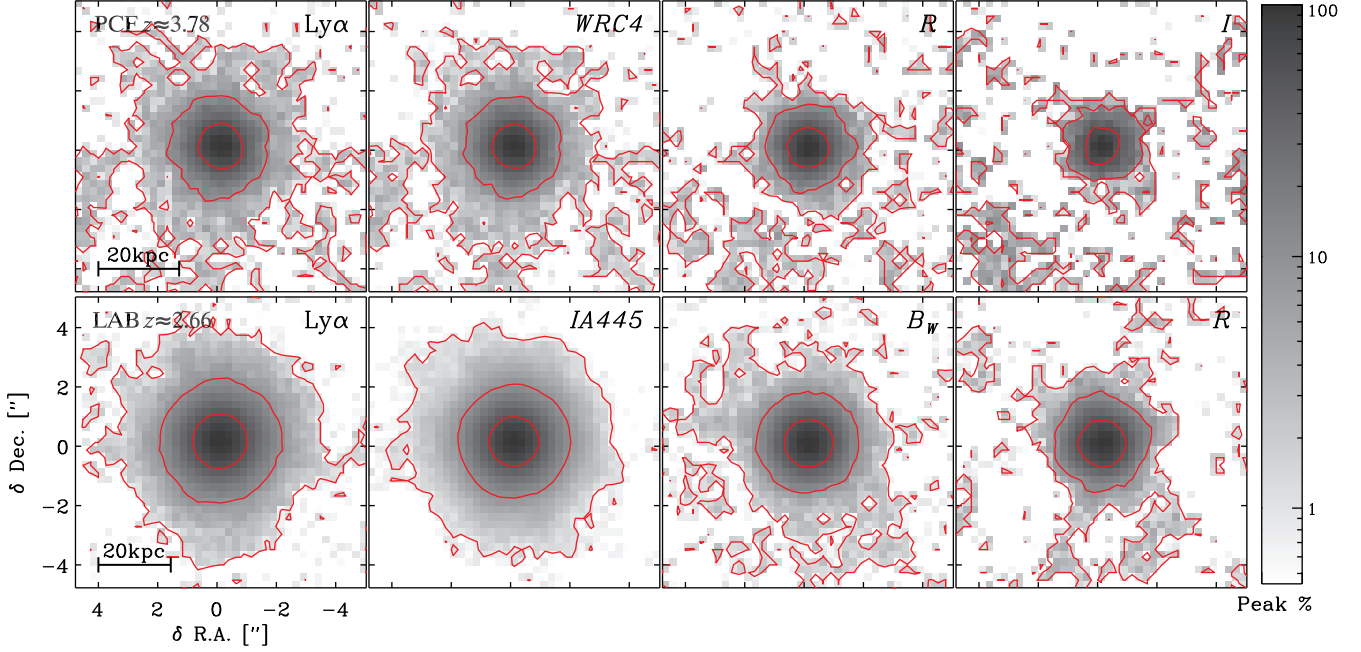


Figure 3. The stacked images of the LAEs in the PCF (top) and LAB (bottom) fields are shown. All images are produced by taking the pixel-to-pixel median of the resampled individual cutouts centered on the galaxy positions and the Ly α images are derived from the difference between the narrow- and broad-band data (see descriptions in §3.2). For the PCF (LAB) sample, the *WRC4* and *R* (*IA445* and *B_W*) bands contain the Ly α and continuum emission near $\lambda_{\text{rest}} \approx 1220\text{\AA}$, while the *I* (*R*) band samples the UV continuum at $\lambda_{\text{rest}} \approx 1700\text{\AA}$. For each image, the red contours show the positions at which the surface brightness falls to 50, 10, 1% of the peak value. The peak-normalized intensity scale is indicated by the color bar on right. Diffuse emission is present in the narrow- and Ly α bands of both samples. The angular distance scale is indicated at the bottom left corner of each panel.

to be 5–6 kpc from the median stacking images of all LAEs. We note that the LAB sample does include at least one known Ly α blob LABd05. However, the stacking results are not affected by such case because of their limited contributions in stacking.

Our size measurements are in excellent agreement with similar measurements performed on individual galaxies at $z \sim 3\text{--}6$ (Wisotzki et al. 2016) and with the median values found for $z \sim 3$ LAEs (Feldmeier et al. 2013; Momose et al. 2014). In contrast, the LAH exponential scalelengths of our samples are a factor of 5–6 smaller than that of the “LAE only” sample in S11. Their sample consists of 18 galaxies with measured rest-frame equivalent widths of $\text{EW}_0(\text{Ly}\alpha) \geq 20\text{\AA}$ similar to our PCF LAEs.

In Figure 5, we present the Ly α radial profiles measured from the full LAE samples, together with previous results from S11 and Momose et al. (2014). The radial profile in the central region is dominated by the combination of the median Ly α line luminosity of the galaxies and the image PSF, and thus depends sensitively on the depth and quality of the imaging data. Therefore, we normalize all profiles at 10 kpc (or $\approx 1.3''\text{--}1.4''$) in the figure, and focus on comparing the slope of the outer radial profile. This slope determines the exponential scalelength (as given by Eq. 4). As evident in Figure 5, our

measured profiles agree reasonably with that of Momose et al. (2014) out to 30 kpc, while are clearly at odds with the S11 profile which declines much more slowly than the rest.

The large discrepancy between our results and S11 may be explained if Ly α halo sizes depend on galaxy properties, such as UV continuum luminosities or Ly α luminosities. While the Ly α EW distribution of our PCF sample and that of the S11 sample are comparable, the latter consists of continuum-detected LBGs with the median magnitude of $R = 24.8$ AB, where *R* band samples the rest-frame 1500\AA . In comparison, our LAE samples is detected in the NB filter, and color-selected to have high line EWs regardless of their UV luminosities. The majority of galaxies in the PCF sample are continuum faint ($I \gtrsim 25.5$ AB). Given that galaxies in the S11 samples range in redshift $z = 2.3\text{--}3.1$, cosmological dimming between their galaxies and the PCF redshift of $z = 3.78$ is at the level of 0.4–0.9 mag. Thus, the majority of galaxies in the S11 samples should have both higher Ly α and UV surface brightness than those in our PCF sample even if their spectra are flat ($f_\lambda \propto \lambda^{-2}$). A redder spectrum would make the gap even larger, which is more likely as continuum bright galaxies tend to be redder (e.g. Bouwens et al. 2009). Similarly, our LAB sample galaxies are even fainter in the absolute UV

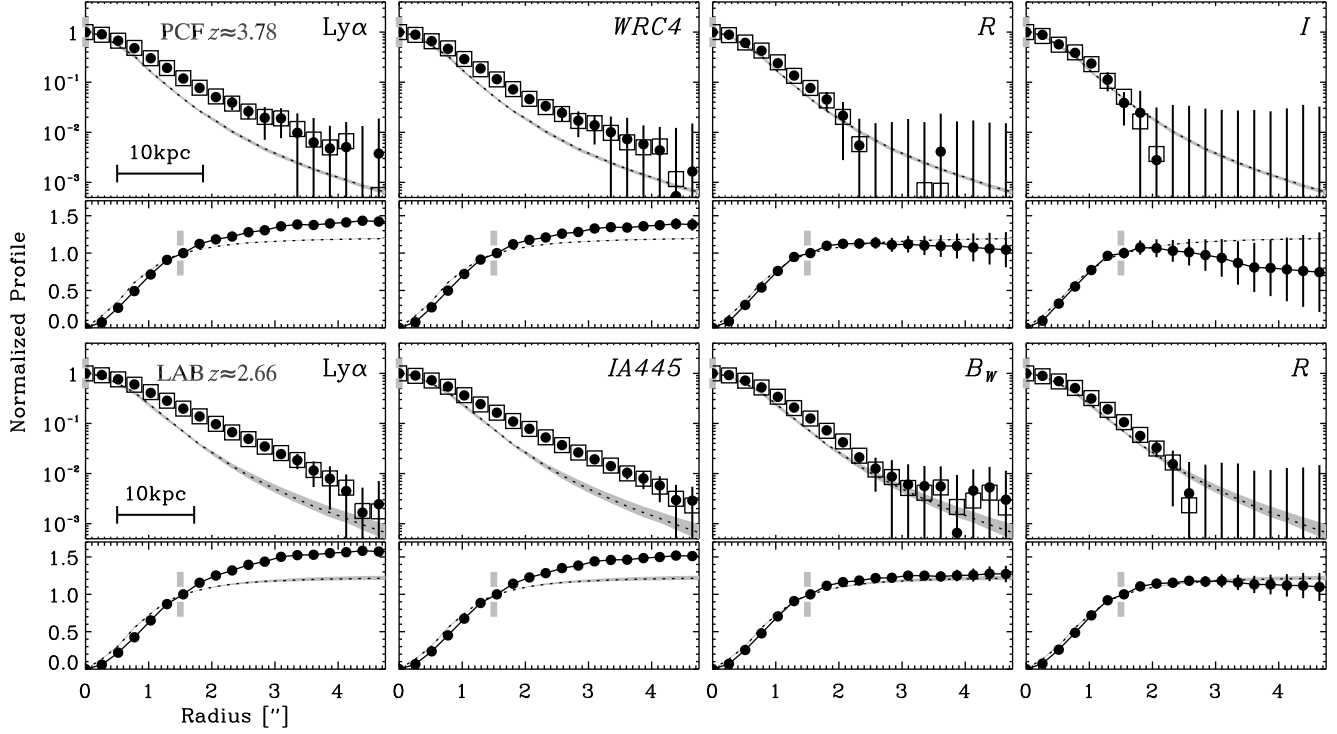


Figure 4. The radial profiles of stacked images presented in Figure 3. For each band, we show both differential and cumulative profiles, normalized at the center and $r = 1.5''$ (indicated by the gray bars), respectively. The differential radial profile is measured by taking median (filled circles) and mean (open squares) in each annulus bin. For comparison, the normalized stellar PSFs are shown as dotted black lines. Gray shades indicate the variations of homogenized PSFs among different pointing and bands. The angular distance scale is indicated at the bottom left corner of each panel.

brightness with a median $M_{UV} \gtrsim -20.2$. The studies by Feldmeier et al. (2013) and by Momose et al. (2014) reported that halo sizes may increase with decreasing Ly α EWs and with increasing UV luminosities (but see Wisotzki et al. 2016), lending further support to this possibility.

It is also conceivable that halo size changes with local environments or evolve with redshift. Notably, Matsuda et al. (2012) analyzed LAHs in bins of LAE surface overdensities (Σ_g), and reported that Ly α halo size scales as $r_n \propto \Sigma_g^2$. Their ‘field’ LAEs have halo sizes of 8–11 kpc, considerably smaller than ~ 20 kpc for the LAEs in the highest overdensity region. Such a dependence may also simultaneously explain the larger LAHs around the S11 sample galaxies, which exclusively reside in massive protoclusters. Wisotzki et al. (2016) measured the LAH sizes of individual LAEs in their sample, and reported that the LAHs around $z \sim 3.7$ LAEs are a factor of ~ 2 larger than those around $z \sim 5.1$ LAEs. However, their sample spans a wide range of Ly α equivalent widths, UV and Ly α luminosities (and of an unknown range of galaxy overdensities), making it difficult to interpret whether the observed trend is a result of redshift evolution, or of varied physical properties of these LAEs at different redshifts.

We note that these different scenarios may not be independent from one another. For example, galaxies residing in overdense regions may have enhanced Ly α or UV luminosities compared to those in underdense or field environment (e.g., Koyama et al. 2013; Lemaux et al. 2014; Dey et al. 2016). Analyses on large and well-controlled subsamples representing different galaxy properties will be crucial to further investigate the primary driver that determines LAH sizes, and thereby constrain the physical origin of LAHs, which is the subject of §5. As a caveat, we also explore how different stacking methods and data characteristics may impact the shape of the surface brightness profiles and LAH scalelengths in Appendices B and C. These investigations are not directly related to the physical properties of LAHs, but crucial in quantifying the robustness of the measurements and associated uncertainties, as well as in understanding the possible origin of discrepancies found among different results in the literature.

It is interesting to consider how our scalelength measurements of high-redshift LAEs compare with those of local Ly α emitting galaxies. Hayes et al. (2013)

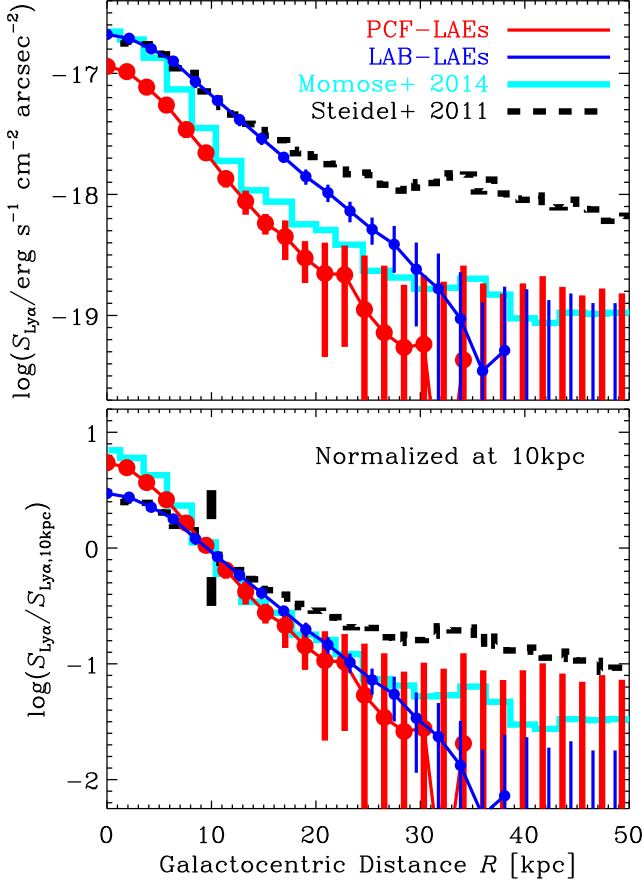


Figure 5. We show the average Ly α radial profiles of our PCF-LAE (red) and LAB-LAE (blue) samples, together with similar measures in the literature: the $z = 3.1$ LAE sample from Momose et al. (2014) (cyan) and the “LAE-only” sub-sample from S11 (gray). All measures are presented in their original forms, including varying degrees of blurring due to the respective image PSFs. *Top:* the surface brightness levels are in physical units. Differences in the overall amplitudes reflect the sample variation in intrinsic Ly α luminosities and cosmological dimming. *Bottom:* The same profiles are normalized at 10 kpc to facilitate comparison of their overall profiles outside the central galaxy (see text). Both of our samples have profiles similar to that measured by Momose et al. (2014) from 10 kpc and 30 kpc.

measured the Petrosian radii⁵ (Petrosian 1976), $R_{P20}^{Ly\alpha}$, for 14 galaxies in their Lyman Alpha Reference Sample (LARS, hereafter), and found that they range in 3 – 15 kpc. Because the authors published only the Petrosian radii and not the two- and one-dimensional light profiles, it is not straightforward for us to make direct

⁵ In Hayes et al. (2013), it is specifically defined as the radius at which the local surface brightness is 20% the average surface brightness inside

comparisons of their measurements to our scalelengths. By assuming that the intrinsic profiles are radially symmetric and decline exponentially with projected galactocentric distance, we find an exponential profile with a scalelength of 6 kpc corresponds to $R_{P20}^{Ly\alpha} \approx 22$ kpc. On the other hand, we estimate values of $R_{P20}^{Ly\alpha} \approx 18 - 22$ kpc by directly computing from our stacked Ly α images obtained at lower physical resolutions. Hence, high-redshift LAEs in our sample appear to have somewhat more extended LAHs than the LARS galaxies. However, we caution that our $R_{P20}^{Ly\alpha}$ estimates are only approximate and more likely upper limits, because properly accounting for the PSF blurring effect and adding a compact galaxy-like Ly α -emitting component (instead of a single exponential profile) may lead to smaller Petrosian radii.

4. CHARACTERIZING GALAXY ENVIRONMENTS

Galaxies in our sample reside in a wide range of environments, including at least three massive protoclusters (Dey et al. 2005; Prescott et al. 2012; Lee et al. 2014; Dey et al. 2016, also § 2). Hence, we are well positioned to explore how the LAH characteristics depend on local galaxy density. We begin by estimating the local LAE density for each sample.

4.1. Estimation of Local LAE Overdensities

As for the PCF sample, the filter width of the NB filter corresponds to an effective line-of-sight distance of 27 Mpc comoving (or 5.6 Mpc physical), qualitatively comparable to the expected size of (unvirialized) forming clusters at the same redshift (Chiang et al. 2013). Moreover, the redshift distribution of PC 217.96+32.3 peaks sharply close to the value corresponding to the central wavelength of the NB filter (Dey et al. 2016). Hence, the use of surface overdensity with smoothing scales of FWHM=5–10 Mpc is well justified as a proxy for the three-dimensional overdensity with minimal contamination by foreground and background interlopers.

We determine the surface overdensity, Σ_{LAE} , as a function of image positions as the following. First, the two dimensional LAE distribution map is smoothed with a Gaussian kernel of FWHM=10 Mpc (or $\sigma = 2'$). Second, the *field* LAE density, $\bar{\Sigma}_{LAE}$, is estimated by dividing the number of LAEs within the effective area (excluding masked regions) after removing the sources likely associated with PC 217.96+32.3. As detailed in Dey et al. (2016), our estimate of the mean LAE density is roughly twice as large as that expected in the field based on integrating the $z \sim 3.7$ Ly α luminosity function determined by Ouchi et al. (2008). Thus, our estimate of the overdensity is likely a conservative one. Finally, the LAE surface overdensity is computed as:

$$\delta_{LAE} = \frac{\Sigma_{LAE} - \bar{\Sigma}_{LAE}}{\bar{\Sigma}_{LAE}}. \quad (7)$$

While all galaxies, including LBGs, are assigned an overdensity parameter based on their image positions, the overdensity itself is determined solely based on the angular distribution of LAEs.

For the LAB sample at $z \approx 2.66$, the same technique is unlikely to yield galaxy overdensity parameters in a meaningful manner. The intermediate filter *IA445*, used to identify photometric candidates of LAEs at $z \approx 2.66$, spans a line-of-sight distance of 190 Mpc, and thus the shot noise from interlopers is expected to play a more significant role in the measured surface overdensity. Therefore, we decide to limit our analyses to the spectroscopic sample and estimate galaxy overdensity in a three dimensional comoving volume using the following procedure: first, we construct a 3D LAE map based on their image positions and redshift, assuming the measured $\text{Ly}\alpha$ redshift as systemic redshift; second, the map is smoothed with a 3D Gaussian kernel of FWHM=20 Mpc; finally, a 3D overdensity, δ_{LAE} , is computed using an equation similar to Eq. 7.

As described in §2, our Hectospec observations resulted in a relatively uniform spectroscopic coverage only in the middle two thirds of the field. The remaining region, namely the eastern and western end of the field totaling $\sim 0.3 \text{ deg}^2$ in area, is excluded from our 3d overdensity measurements and subsequent analysis.

The use of $\text{Ly}\alpha$ redshift in determination of their line-of-sight position can lead to an error in our overdensity estimation. However, such uncertainties are likely negligible in the present case. A typical offset between $\text{Ly}\alpha$ -derived and systemic redshift is $\Delta z = 0.003\text{--}0.004$ or $250\text{--}330 \text{ km s}^{-1}$ in velocity space. These offsets will lead to the positional error of $3.4\text{--}4.6 \text{ Mpc}$ comoving, much smaller than the adopted smoothing scale of 20 Mpc. More reliastically, the positional error is even smaller than the above values as most LAEs should have their $\text{Ly}\alpha$ line shifted in the same direction with similar magnitudes.

In Figure 1, we show the overdensity properties of both PCF field (left) and LAB field (right), together with the positions of individual sources in each sample, color coded by redshift for the spectroscopic sources. For the PCF field, both contours and orange shades indicate the surface overdensity levels, clearly marking two spectroscopically confirmed structures located at center and northeastern corner of the PCF field (Lee et al. 2014; Dey et al. 2016). Many LBG members of the structures are also marked (although they are not included in the overdensity estimate shown as contours and shades). In the LAB field (right panel of Figure 1), we show the second moment of the three-dimensional overdensities as orange shades. The highest overdensity region ($\delta_{\text{LAE}} \gtrsim 5$) is located slightly off center in the southeastern direction, coinciding with the position of the $\text{Ly}\alpha$ blob, LABd05, marked as large open square (Dey et al. 2005).

Our choices of smoothing kernels (10 Mpc and 20 Mpc for the PCF and LAB samples, respectively) are justified by the observed surface density of LAEs in these fields. A smoothing kernel size – i.e., the effective volume within which the galaxies are counted – should be large enough to enclose a relatively large number galaxies to minimize shot noise in the overdensity estimate. The transverse distance to the nearest neighbor for the PCF sample ranges from 0.3 Mpc to 9.7 Mpc with a median value of 2.7 Mpc. As for the LAB sample, the total (transverse) distance to the nearest neighbor spans 0.7 (0.4) Mpc to 31.5 (18.1) Mpc with the median of 7.8 (4.5) Mpc. Our adopted kernels are large enough to enclose at least one LAE in the least concentrated region.

4.2. Calibration of Local Overdensities

The above overdensity estimates should be a good relative measure to distinguish overdense or underdense regions within a single field. However, they are inadequate to be compared with one another or with similar measures in other surveys, because measured overdensity is generally a function of smoothing scale, imaging or spectroscopic depth of the survey, and filter-determined redshift range (e.g. Chiang et al. 2013). A larger smoothing kernel (2D or 3D) would effectively average over more galaxies, reducing the shot noise of the overdensity measure at the expense of washing out features that are smaller than the size of the kernel. Conversely, using too small a kernel would exaggerate the overdensity parameter. A broader NB filter would increase the shot noise from unassociated sources in the foreground and background, washing out the signal from a coherent structure. The imaging and spectroscopic depth not only influence the overall error budget due to shot noise but also determine the average bias of the galaxy population uncovered as a result of such a survey. Depending on the specifics of a galaxy density structure and how it is observed, a range of overdensity parameters is expected for the same structure.

To facilitate direct comparison of our PCF and LAB results with other measurements in the literature, we calibrate our overdensity estimates using a simulated $z \sim 3$ galaxy catalog of Chiang et al. (2013), which is based on the Millennium I and II Simulation Runs (Springel et al. 2005). Their catalog provides sky positions and redshift of individual galaxies with star formation rates $\geq 1 M_{\odot}/\text{yr}$, comparable to typical values measured for LAEs (e.g., Gawiser et al. 2006; Guaita et al. 2010). Specifically, we first derive galaxy overdensities measured using a tophat cubic box with 15 Mpc on a side. Second, each simulated galaxy is assigned an overdensity parameter accordingly. Third, we repeated the step #1 and #2 using a series of smoothing kernels closely matching those used in our data and also those used by Matsuda et al. (2012) and Momose et al. (2016) as listed in Table 1. We denote the respective overdensity parameters as $\delta_{\text{sim}}^{\text{PCF}}$, $\delta_{\text{sim}}^{\text{LAB}}$, $\delta_{\text{sim}}^{\text{M12}}$, and $\delta_{\text{sim}}^{\text{M16}}$.

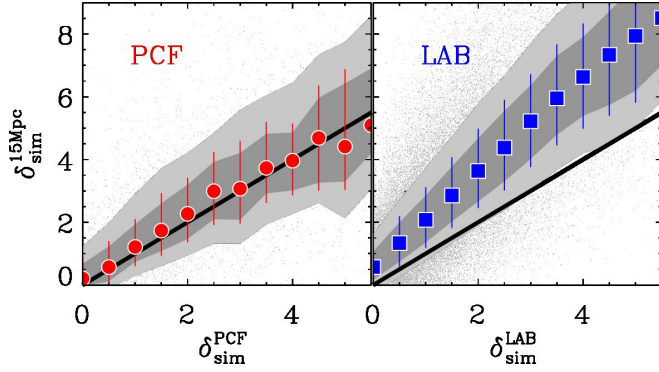


Figure 6. Calibration of measured galaxy overdensities: Utilizing the full Millennium Runs volume, we determine local galaxy overdensities using smoothing kernels designed to match that used in the real data, and compare them to those determined within a $(15 \text{ Mpc})^3$ tophat cubic volume, δ_{sim}^{15Mpc} . Dark gray shades bracket the 30–70% range, while lighter gray shades mark the 15–85% range. In both panels, thick black line marks the one-to-one line. The correction factor derived from the median relation is later used to bring all measured overdensities in real data to a common standard.

Following Chiang et al. (2013) who used the overdensity measured in a 15 Mpc cubic box to evaluate the significance of a protocluster, we adopt δ_{sim}^{15Mpc} as a benchmark, and determine how other measures map into it. In Figure 6, we show the distribution of overdensity parameter of all simulated galaxies on the δ_{sim}^{15Mpc} – δ_{sim}^{PCF} (left) and δ_{sim}^{15Mpc} – δ_{sim}^{LAB} plane (right). The δ_{sim}^{PCF} parameter is close to our benchmark: the reason is that the larger line-of-sight distance (25 Mpc) and smaller kernel size (10 Mpc FWHM) together effectively enclose a cosmic volume similar to our benchmark measure. On the other hand, the δ_{sim}^{LAB} parameter yields a systematically lower value than the benchmark mainly due to the larger smoothing scale (20 Mpc FWHM). The same procedure is carried out for the Matsuda et al. (2012) and Momose et al. (2016) estimates, and all overdensity parameters measured from real data are converted to the benchmark values δ_{sim}^{15Mpc} .

5. DEPENDENCE OF LAHS ON GALAXY PROPERTIES

We now investigate how the LAH properties depend on local environment, Ly α luminosities and equivalent widths, and UV continuum luminosities. Local overdensities are measured as a function of image positions (detailed in § 4), then each galaxy in our sample is assigned an overdensity based on their image positions. Because all of our samples are LAEs (except the small number of LBGs in the PCF field) and confined into narrow

redshift ranges⁶, their UV luminosities, Ly α luminosities, and line equivalent widths can be ranked by their CB brightness, NB magnitudes, and NB–BB colors, respectively. Based on the directly measured parameters, we subdivide our samples accordingly and repeat the image stacking and profile measurement procedures as described in § 3.2.

In Tables 3 and 4, we list the criteria and size of each subsample in the PCF and LAB field, respectively. The distributions of galaxy properties and subsample boundaries are presented in Figure 7. Also shown in the tables are the best-fit scalelengths using both exponential model and two-component model (see Eq. 4 and Eq. 5 in § 3.2). There is a tendency the exponential scalelength, r_s , is slightly larger than the two-component scalelength, $r_{s,h}$. The former does not explicitly account for the PSF, and thus can be sensitive to the exact PSF shape at outer radii. More extensive discussion on this subject is given in Appendix C. We also present the physical properties of each subsample in Tables 3 and 4 – Ly α luminosity, equivalent width, and UV luminosity. The absolute UV magnitudes are computed from the broadband brightness near the rest-frame wavelengths 1700Å (assuming $f_\lambda \propto \lambda^{-2}$), over an aperture of radius $r = 2''$. The Ly α luminosities and rest-frame EWs within a $r = 3''$ aperture are derived fully taking into account the filter response and intergalactic absorption, as detailed in Appendix A. The slightly larger aperture is chosen to capture the total Ly α flux of stacked objects (see the cumulative Ly α light profile in Figure 3). These values are derived directly from the stacked images of individual subsamples, but agree with the median of the same quantities determined individually from each galaxy.

5.1. Local Environments

In Figure 8, we show the scalelengths of our LAE subsamples as a function of local overdensity in comparison to the exponential scalelengths measured by Matsuda et al. (2012) and by Momose et al. (2016). The exponential and two-component scalelengths are indicated as open and filled symbols, respectively. As detailed in § 4, we adjust all measured overdensities in this work and those in Matsuda et al. (2012) to the benchmark δ_{sim}^{15Mpc} , i.e., the three-dimensional overdensity measured in a tophat $(15 \text{ Mpc})^3$ volume. As evident in Figure 8, both of our samples contain overdensities comparable to those examined by Matsuda et al. (2012), which appear as regions of darker shade in Figure 1.

We do not find any correlation between measured scalelengths and overdensity parameters in both of our datasets. Regardless of the measured overdensities, all

⁶ The luminosity estimation should be robust even for the non-spectroscopic LAEs in the LAB field ($z = 2.569\text{--}2.737$) as the redshift uncertainty only leads to a brightness error of ≈ 0.11 mag.

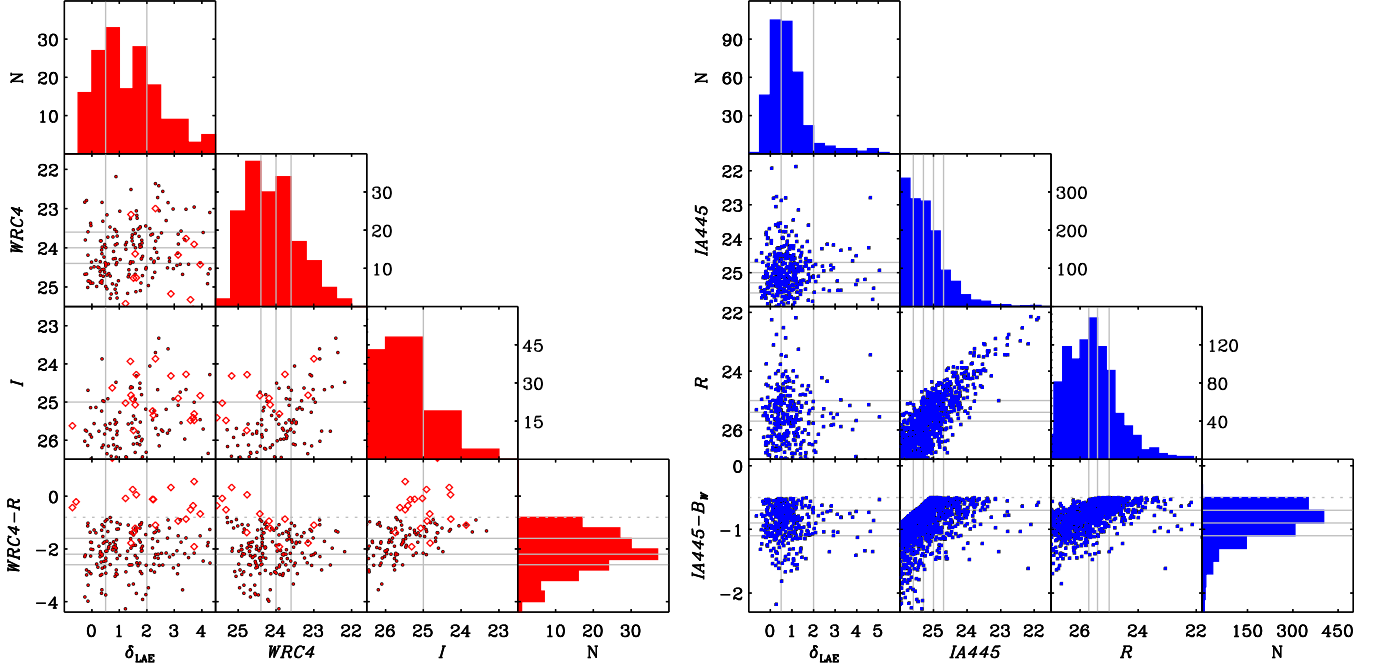


Figure 7. Distributions of measured galaxy properties within our PCF (red) and LAB (blue) LAE samples: namely, LAE overdensities, NB/CB magnitudes, and NB–BB colors. For the PCF sample, the properties of the spectroscopically confirmed LBGs at the same redshift are indicated as open diamonds. Solid gray lines represent the divide between subsamples as described in § 5. In both samples, a positive correlation exists between NB and CB magnitudes, which is a bias from LAE color selection criteria (see, e.g. Ciardullo et al. 2012).

subsamples have LAH sizes of $\sim 4\text{--}6\text{ kpc}$, similar to the LAEs residing in field environment ($\delta \approx 0$) as reported by Momose et al. (2016). The lack of correlation with overdensity parameter is in clear tension with the Matsuda et al. (2012) results. The reason for this disagreement is unclear. The LAE selection technique in Matsuda et al. (2012) are similar to ours, and so are the measured median properties of their subsamples: i.e., Ly α equivalent widths, continuum and Ly α luminosities.

However, we note that their high-overdensity subsamples also exhibit higher Ly α luminosities measured with isophotal apertures determined on the Ly α images. This trend only weakly exists in our PCF sample (see Table 3 here, or Figure 11 in Dey et al. 2016), and is not present in the LAB sample. Another difference between the Matsuda et al. (2012) sample and ours is that the former consists of LAEs in four independent fields (GOODS-N, SDF, SXDF, and SSA22) while both of our sample galaxies reside in a contiguous field. While it is unclear how many LAEs in their highest overdensity sample reside in each of their fields (not published), it is possible their sample is dominated by one particular field, SSA22, in which very large LAHs around UV-luminous galaxies and numerous Ly α blobs are found around a very significant galaxy overdensity (Steidel et al. 2000; Matsuda et al. 2004; Steidel et al. 2010). In contrast, the protocluster in the PCF field has spectroscopically confirmed LAE overdensity that is as large as that found in

the SSA22 structure while no Ly α blob is present in the entire field. The characteristics of the LAB field lie in the middle between those of the PCF and SSA22 structures, and we also excluded the very luminous Ly α blob (LABd05) identified in (Dey et al. 2005) in the highest overdensity subsamples. It is not clear the contribution of Ly α blobs in the LAH characteristics in the stacking result of Matsuda et al. (2012). But our test of including LABd05 does suggest the LAH scalelength from two-component fit could increase to $r_{s,h} = 5.1^{+1.7}_{-1.2}$ to $6.0^{+1.6}_{-1.3}$, leading to a weak positive correlation between the LAH scalelength and overdensity. Careful and uniform re-analyses of all protocluster data and a study based on larger samples of protocluster systems in the future are required to understand the relative significance of Ly α blobs in the averaged galaxy Ly α halo properties.

5.2. UV Luminosities

The average LAH sizes increase with UV luminosity in both of our galaxy samples (Figure 9, middle). At the lowest luminosities, $M_{UV} \approx -(18\text{--}19)$, the measured scalelengths range in $4\text{--}5\text{ kpc}$, similar to those reported by Wisotzki et al. (2016) for individual LAEs of comparable continuum luminosities. However, the LAH size in $r_{s,h}$ doubles from 4.2 kpc to 8.6 kpc for the lowest to highest luminosity bin in the LAB sample.

To evaluate the significance of this correlation, we use SAFE_CORRELATE routine in the IDL Astronomy Users Library. The routine can simulate new realizations of

Table 3. PCF Subsamples and Their Average Continuum and LAH Properties

Name	Selection	N^a	$\log(L_{\text{Ly}\alpha})^b$ (erg s $^{-1}$)	M_{UV}^c	EW_0^d Å	r_s (kpc)	$r_{s,h}$ (kpc)	$r_{s,c}^e$ (kpc)
LBG	Eq. 2 (§ 2.1)	21	42.42	$-21.24^{+0.17}_{-0.15}$	10^{+5}_{-3}	$7.5^{+6.3}_{-3.7}$	$5.8^{+5.2}_{-1.3}$	1.3
LAE	Eq. 1 (§ 2.1)	163	42.72	$-19.79^{+0.14}_{-0.13}$	70^{+14}_{-11}	$5.7^{+0.7}_{-0.5}$	$4.8^{+0.4}_{-0.9}$	1.2
LAE-env-s1	$2.0 \leq \delta_{\text{LAE}}$	44	42.87	$-20.32^{+0.20}_{-0.16}$	67^{+12}_{-10}	$5.5^{+1.0}_{-0.8}$	$5.2^{+1.4}_{-0.9}$	1.7
LAE-env-s2	$0.5 \leq \delta_{\text{LAE}} < 2.0$	76	42.75	$-19.47^{+0.25}_{-0.21}$	87^{+14}_{-11}	$7.2^{+1.4}_{-1.1}$	$7.0^{+2.1}_{-2.5}$	1.4
LAE-env-s3	$\delta_{\text{LAE}} < 0.5$	43	42.72	$-19.24^{+0.45}_{-0.25}$	100^{+40}_{-24}	$4.2^{+2.3}_{-0.7}$	$3.9^{+1.9}_{-0.6}$	0.9
LAE-Ly α -s1	$WRC_4 < 23.6$	36	43.08	$-20.81^{+0.15}_{-0.11}$	67^{+12}_{-9}	$7.2^{+1.2}_{-1.0}$	$7.0^{+1.5}_{-1.1}$	1.5
LAE-Ly α -s2	$23.6 \leq WRC_4 < 24.0$	34	42.84	$-19.18^{+0.27}_{-0.22}$	113^{+35}_{-28}	$7.4^{+1.1}_{-0.9}$	$8.6^{+3.7}_{-2.9}$	1.5
LAE-Ly α -s3	$24.0 \leq WRC_4 < 24.4$	29	42.74	$-19.79^{+0.48}_{-0.33}$	68^{+21}_{-14}	$4.7^{+2.2}_{-1.4}$	$3.5^{+2.1}_{-1.3}$	1.1
LAE-Ly α -s4	$24.4 \leq WRC_4$	64	42.57	$-19.06^{+0.59}_{-0.38}$	73^{+39}_{-22}	$3.8^{+0.5}_{-1.1}$	$2.5^{+0.4}_{-0.7}$	0.9
ALL-UV-s1	$I < 25.0$	19	42.88	$-21.58^{+0.07}_{-0.07}$	20^{+5}_{-4}	$6.9^{+1.2}_{-1.5}$	$5.5^{+2.7}_{-0.6}$	1.3
ALL-UV-s2	$25.0 \leq I$	161	42.74	$-19.71^{+0.14}_{-0.12}$	72^{+11}_{-9}	$5.4^{+1.1}_{-0.4}$	$3.7^{+0.9}_{-0.5}$	1.1
LAE-EW-s1	$WRC_4 - R < -2.6$	44	42.74	$-17.65^{+0.89}_{-0.55}$	242^{+370}_{-165}	$3.9^{+0.5}_{-0.4}$	$2.8^{+0.3}_{-1.2}$	1.0
LAE-EW-s2	$-2.6 \leq WRC_4 - R < -2.2$	28	42.80	$-19.20^{+0.52}_{-0.42}$	136^{+74}_{-36}	$5.9^{+2.9}_{-1.8}$	$4.2^{+2.4}_{-0.8}$	0.9
LAE-EW-s3	$-2.2 \leq WRC_4 - R < -1.6$	47	42.82	$-19.93^{+0.20}_{-0.15}$	70^{+9}_{-7}	$8.2^{+1.2}_{-1.1}$	$9.9^{+2.3}_{-2.4}$	1.8
LAE-EW-s4	$-1.6 \leq WRC_4 - R$	44	42.76	$-20.85^{+0.7}_{-0.6}$	32^{+5}_{-3}	$6.2^{+1.2}_{-1.0}$	$4.4^{+1.0}_{-1.1}$	1.4

^a The total number of galaxies considered in stacking analyses.

^b Average Ly α luminosity integrated over a $r=3''$ aperture in the stacked image. The typical uncertainty is ~ 0.02 dex base on the image statistical noise. However, the uncertainty in the LBG subsample reaches 0.1 dex.

^c Absolute UV magnitude derived from the integrated flux in the stacked I -band image, over a $r=2''$ aperture. The error represents the statistical uncertainty in the stacked image.

^d Rest-frame photometric EW derived from the $WRC_4 - R$ color of the stacked object, measured in a $r=3''$ aperture. The error represents the uncertainty propagated from the stacked image noise.

^e All UV continuum light profiles are consistent with the expectation from a point source. The pixel size of $0.258''$ is equivalent with an angular size of 1.9 kpc at $z = 3.78$.

scaleglengths based on the measured values and their uncertainties, and then determine the overall probability that the apparent $r_{s,h}-M_{\text{UV}}$ trend could be due to statistical fluctuations. For the LAB sample, the test suggests a low probability of the null hypothesis ($\sim 9\%$). For the PCF sample, SAFE_CORRELATE (which is based on the Spearman rank correlation) can not provide useful insight on the correlation significance because we only have two subsamples due to the limited dynamics range in the sample UV luminosity. However, the positive correlation trend between $r_{s,h}$ and M_{UV} still holds.

We also stack 21 LBGs in the PCF field with spectroscopic redshifts – many of which are also UV-bright LAEs – and find similar two-component and exponential scaleglengths of 7.5 kpc and 5.8 kpc, respectively. However, we note that the measurements for both UV bright LAEs and LBGs in the PCF sample are limited by a smaller number of galaxies, making the size measurements very uncertain. We carry out Monte Carlo realizations by randomly selecting subsets of LBGs and

stacking them and find a large spread in the measured correlation lengths. In particular, some realizations only containing LBGs with Ly α in emission yield scaleglengths as large as 12 kpc, much larger than our formal best fit of 7.5 kpc. A larger LBG sample is crucial to further test this possibility.

At the highest luminosities probed by both samples ($M_{\text{UV}} \approx -21$), the measured scaleglengths are consistent with those reported by Momose et al. (2016), although they found larger scaleglengths towards lower luminosities of $M_{\text{UV}} \approx -(19-20)$. In Figure 9, we also show the exponential scaleglengths measured by S11 as green data points. Different symbols represent their subsamples binned by the level of Ly α emission or the estimated rest-frame EWs, all of which are considerably more luminous than our samples. We note that Momose et al. (2016) used galaxy properties derived from a $r = 1''$ aperture to subdivide samples. The same photometry is adopted for the M_{UV} values of their subsamples, which

Table 4. LAB Subsamples and Their Average Continuum and LAH Properties

Name	Selection	N^a	$\log(L_{\text{Ly}\alpha})^b$ (erg s^{-1})	M_{UV}^c	EW_0^d Å	r_s (kpc)	$r_{s,h}$ (kpc)	$r_{s,c}^e$ (kpc)
LAE	Eq. 3 (§ 2.2)	1336	42.83	$-19.20^{+0.08}_{-0.08}$	150^{+15}_{-13}	$6.0^{+0.5}_{-0.5}$	$5.7^{+0.6}_{-0.5}$	1.7
LAE-specz	Eq. 3 (§ 2.2)	429	42.89	$-19.36^{+0.05}_{-0.05}$	160^{+24}_{-20}	$5.5^{+0.5}_{-0.4}$	$5.1^{+0.5}_{-0.5}$	1.2
LAE-specz-env-s1	$2.0 \leq \delta$	29	42.90	$-19.14^{+0.24}_{-0.21}$	177^{+57}_{-39}	$4.8^{+1.3}_{-0.9}$	$5.1^{+1.7}_{-1.1}$	0.9
LAE-specz-env-s2	$0.5 \leq \delta < 2.0$	139	42.92	$-19.32^{+0.09}_{-0.10}$	153^{+41}_{-23}	$5.6^{+0.6}_{-0.5}$	$5.5^{+0.7}_{-0.5}$	1.5
LAE-specz-env-s3	$\delta < 0.5$	86	42.94	$-19.30^{+0.14}_{-0.11}$	176^{+29}_{-21}	$5.7^{+0.7}_{-1.6}$	$5.0^{+0.7}_{-0.6}$	1.0
LAE-Ly α -s1	$IA445 < 24.7$	228	43.19	$-20.51^{+0.03}_{-0.02}$	99^{+9}_{-7}	$6.5^{+0.7}_{-0.6}$	$7.6^{+1.1}_{-1.0}$	2.0
LAE-Ly α -s2	$24.7 \leq IA445 < 25.0$	162	42.94	$-19.78^{+0.07}_{-0.06}$	114^{+19}_{-12}	$6.3^{+0.7}_{-0.6}$	$6.0^{+0.9}_{-0.7}$	1.8
LAE-Ly α -s3	$25.0 \leq IA445 < 25.3$	289	42.82	$-19.47^{+0.06}_{-0.06}$	133^{+25}_{-16}	$6.1^{+0.5}_{-0.5}$	$5.2^{+0.5}_{-0.4}$	1.5
LAE-Ly α -s4	$25.3 \leq IA445 < 25.6$	278	42.74	$-18.58^{+0.10}_{-0.09}$	161^{+27}_{-23}	$5.6^{+1.1}_{-0.8}$	$4.5^{+0.9}_{-0.7}$	0.7
LAE-Ly α -s5	$25.6 < IA445$	439	42.60	$-17.71^{+0.28}_{-0.22}$	216^{+34}_{-30}	$5.0^{+0.8}_{-0.6}$	$3.9^{+0.6}_{-0.4}$	0.6
LAE-UV-s1	$R < 25.0$	215	43.14	$-20.71^{+0.03}_{-0.02}$	74^{+11}_{-7}	$7.1^{+0.9}_{-0.7}$	$8.6^{+1.2}_{-1.3}$	2.2
LAE-UV-s2	$25.0 \leq R < 25.4$	162	42.83	$-19.93^{+0.07}_{-0.05}$	90^{+12}_{-10}	$6.4^{+0.7}_{-0.6}$	$5.5^{+0.7}_{-0.6}$	1.8
LAE-UV-s3	$25.4 \leq R < 25.7$	152	42.82	$-19.60^{+0.10}_{-0.08}$	101^{+17}_{-13}	$5.9^{+1.0}_{-0.9}$	$4.7^{+1.5}_{-0.9}$	1.8
LAE-UV-s4	$25.7 \leq R$	723	42.72	$-18.52^{+0.09}_{-0.08}$	228^{+52}_{-44}	$5.4^{+0.5}_{-0.4}$	$4.2^{+0.9}_{-0.7}$	0.6
LAE-EW-s1	$IA445 - B_W < -1.1$	293	42.75	$-17.42^{+0.34}_{-0.21}$	279^{+125}_{-110}	$5.7^{+1.7}_{-1.2}$	$4.6^{+2.1}_{-1.1}$	1.0
LAE-EW-s2	$-1.1 \leq IA445 - B_W < -0.9$	317	42.77	$-18.60^{+0.10}_{-0.07}$	206^{+40}_{-34}	$6.2^{+1.1}_{-0.9}$	$5.2^{+1.2}_{-0.8}$	1.3
LAE-EW-s3	$-0.9 \leq IA445 - B_W < -0.7$	424	42.80	$-19.28^{+0.06}_{-0.05}$	127^{+16}_{-13}	$5.4^{+0.5}_{-0.4}$	$4.5^{+0.5}_{-0.4}$	1.5
LAE-EW-s4	$-0.7 \leq IA445 - B_W$	362	42.90	$-20.11^{+0.04}_{-0.03}$	78^{+12}_{-17}	$6.8^{+0.7}_{-0.5}$	$6.9^{+0.8}_{-0.5}$	2.0

^a The total number of galaxies considered in stacking analyses.

^b Average Ly α luminosity integrated over a $r=3''$ aperture in the stacked image. The typical uncertainty is ~ 0.02 dex base on the image statistical noise.

^c Absolute UV magnitude derived from the integrated flux in the stacked R -band image, over a $r=2''$ aperture.

^d Rest-frame photometric EW derived from the $IA445 - B_W$ color of the stacked object, measured in a $r=3''$ aperture.

^e All UV continuum light profiles are consistent with the expectation from a point source. The pixel size of $0.258''$ is equivalent with an angular size of 2.1 kpc at $z = 3.78$.

we compared with. They may slightly underestimate the galaxy total UV luminosity.

5.3. Ly α Luminosities

We find a positive correlation between LAH size and Ly α luminosity, as evident in the left panel of Figure 9. A test using SAFE_CORRELATE gives the null hypothesis probability of 21% and 8% for the PCF and LAB samples, respectively. At the lowest Ly α luminosities ($\log L_{\text{Ly}\alpha} \approx 42.5$), our measurements are once again fully consistent with the individual size measurements of Wisotzki et al. (2016). In contrast, Momose et al. (2016) reported an opposite trend at low luminosities not probed by our samples: LAH sizes decrease with increasing Ly α luminosities.

Most subsamples from S11 probe the highest luminosity regime at $L_{\text{Ly}\alpha} \gtrsim 10^{43} \text{ erg s}^{-1}$. Their results show that the exponential scalelengths increase with Ly α luminosity, which is similar to our findings. However, their

measured scalelengths are systematically larger than any other studies, which may reflect the fact that their galaxies are selected as LBGs and the majority of them are considerably more luminous in continuum emission.

It is evident in Figure 9 (left) that the observed trend is stronger if the two-component scalelengths $r_{s,h}$ are considered instead of the exponential ones r_s in both cases. We investigate the cause of this difference, and find that the presence of strong compact Ly α emission in the central region (presumably originating from the galaxy itself), can lead to an underestimation of *exponential scalelengths*. We refer the readers interested in further details of this argument to Appendix C. On the other hand, two-component scalelengths should be largely unaffected as long as the PSF effect on the global shape of the LAH is properly taken into account. Hence, it appears that the LAH size depends sensitively on Ly α

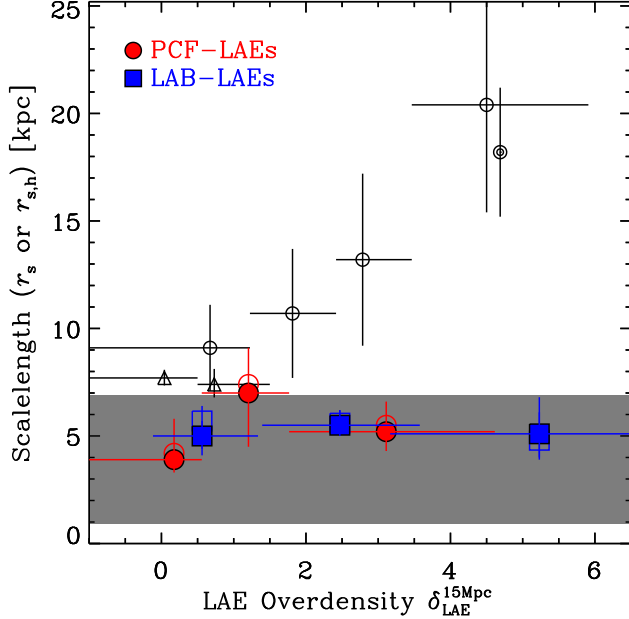


Figure 8. Best-fit LAH scalelengths as a function of LAE overdensity. The scalelengths are measured by fitting surface brightness profiles to a single-component exponential model or a two-component model, denoted as r_s (open symbols) or $r_{s,h}$ (filled symbols). Our measurements are presented in red (PCF) and blue (LAB) symbols, and the results of Matsuda et al. (2012) and Momose et al. (2016) are shown in black open circles and triangles, respectively. The gray shade indicates the LAH scalelength range measured from individual galaxies in Wisotzki et al. (2016). We note that Matsuda et al. (2012) and Momose et al. (2016) adopted the single-component exponential model for scalelength fit, and the values of Wisotzki et al. (2016) are from two-component modeling.

luminosities; nearly doubling the characteristic size from the lowest to highest luminosity bin.

We suspect that the LAH size dependence on Ly α luminosity and on UV luminosity are likely connected. Because the LAE color selection criteria sets the minimum Ly α EW for any galaxy to be selected as an LAE, more continuum luminous galaxies need to have higher Ly α luminosities to meet the criteria, thus creating an artificial positive correlation between the UV and Ly α luminosities (Figure 7; also see, e.g. Ciardullo et al. 2012). Indeed, in our samples, the Ly α luminosities and UV continuum luminosities of individual galaxies are positively correlated albeit with large scatter as can be seen in the median values for different subsamples presented in Tables 3 and 4. These considerations suggest that the observed correlation with Ly α luminosities is at least in part influenced by this selection effect.

5.4. Ly α Equivalent Widths

No clear correlation between LAH sizes and Ly α equivalent widths is found in our sample (Figure 9, right). The null hypothesis probability reaches above 40% for both PCF and LAB samples. Once again, our measured scalelengths are similar to those of Wisotzki et al. (2016), while generally lying below the values reported by Matsuda et al. (2012) and Momose et al. (2016). The former observed a very weak trend of lower-EW galaxies having slightly larger halos (8.3 kpc and 10.5 kpc for the highest- and lowest-EW sample, respectively). The measurements from S11 populate the low end of the EW range as they are UV-luminous LBGs, and their large scalelengths likely reflect their high continuum luminosities.

Based on the above considerations, we postulate that UV-bright galaxies are likely to have larger LAHs, while Ly α luminosities and EWs, which themselves correlate with UV luminosities, produce weaker correlations with the scalelengths. This interpretation is similar to that suggested by Feldmeier et al. (2013) and Momose et al. (2016), that the galaxies whose properties are closest to those of Lyman-break galaxies appear to have the most extended Ly α halos. LBGs, compared to LAEs, generally have higher UV continuum luminosities, EWs, and redder spectral slopes. In this scenario, the general discordance between different measurements can be partly explained: the Wisotzki et al. (2016) measures lie lower than the most because their galaxies are the least UV luminous; the very large scalelengths measured by S11 reflect the fact that their galaxies are much more continuum luminous than other samples.

We note that the equivalent widths in our samples, measured individually and on average, are generally within the limit of the “Case B” recombination dust-free assumption, i.e., $\lesssim 240\text{\AA}$ (Charlot & Fall 1993). Although the subsamples with the strongest NB–BB color apparently show photometric EWs exceeding $\approx 200\text{\AA}$, their uncertainties are significantly larger due to poor constraints on the UV continuum near $\lambda_{\text{rest}} \approx 1220\text{\AA}$. Although our spectroscopic observations do not indicate AGN contamination in our samples, it is possible that some galaxies in our samples may contain AGN. The median-combination stacks we use should reject such sources as long as the majority of LAEs do not harbor AGN. Previous studies also suggest a relatively low AGN contribution to the LAE population at $z < 4$ (e.g. Gawiser et al. 2006; Nilsson et al. 2009). Therefore, there is no clear evidence of other Ly α generation mechanisms rather than the recombination radiation from star formation.

6. THE ORIGIN OF LYMAN ALPHA HALOS: DISCUSSIONS AND COMPARISON WITH THEORETICAL MODELS

Apart from the fact that the resonant scattering nature of Ly α photons provides a mechanism to produce extended LAHs, there is no general consensus in the lit-

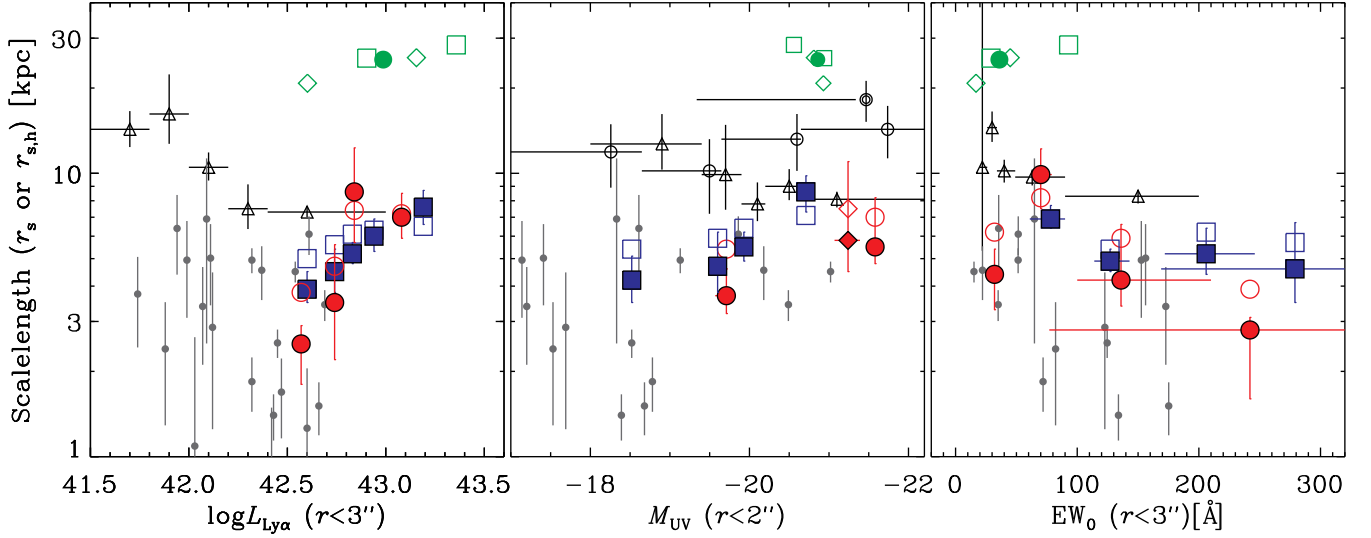


Figure 9. LAH scalelengths as a function of $\text{Ly}\alpha$ luminosities (left), absolute UV magnitudes (middle), and $\text{Ly}\alpha$ equivalent widths (right). Scalelengths are measured by fitting the azimuthally averaged surface brightness profile to a single-component exponential model and a two-component model, denoted as r_s (open symbols) and $r_{s,h}$ (filled symbols), respectively. In each panel, our PCF and LAB measurements are shown in red and blue, respectively. Also shown are exponential scalelengths r_s measurements from S11 (green symbols), Matsuda et al. (2012) (black open circles), Momose et al. (2016) (black open triangles), and Wisotzki et al. (2016, dark gray filled circles). We note that we adopt the same aperture ($r=3''$) as Wisotzki et al. (2016) for measuring $\text{Ly}\alpha$ -related galaxy physical properties. The other studies adopted slightly different apertures (NB-based isophotal apertures for S11 and Matsuda et al. (2012), and $r=1''$ apertures for Momose et al. (2016)).

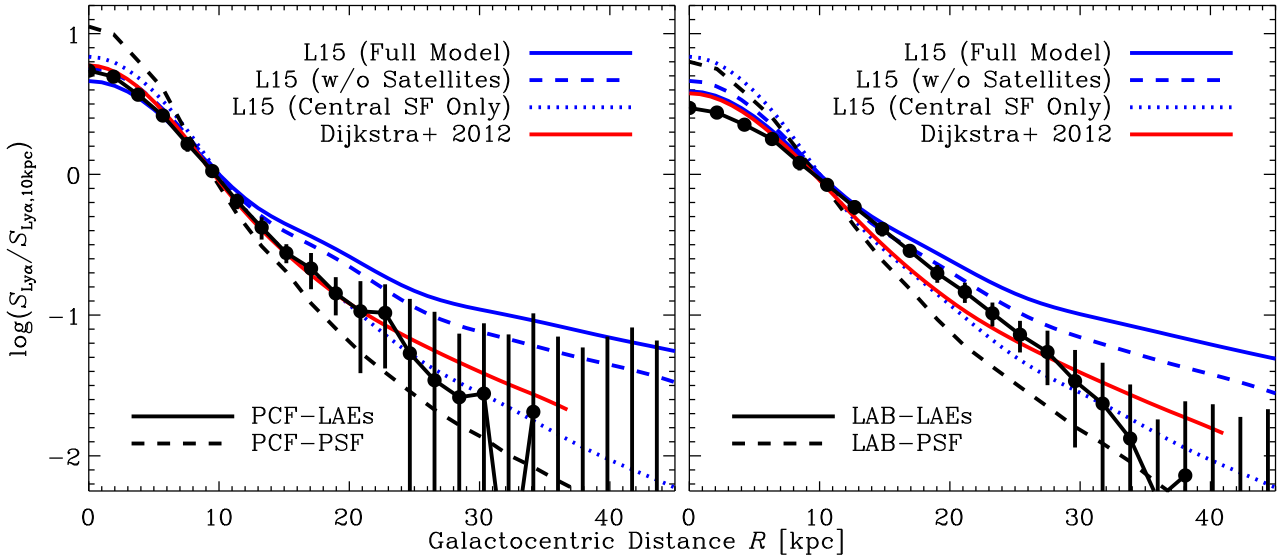


Figure 10. The measured LAH radial profiles are compared with theoretical predictions. All curves are normalized at 10 kpc to compare the slope at larger radii. Our measurements, shown in black, are based on the full LAE samples in the PCF (left) and LAB (right) field. The PSF measured from the image is also indicated in gray. Theoretical models are convolved with the PSFs then normalized at 10 kpc for fair comparison. Three models presented in Lake et al. (2015) are indicated in blue; their full model (solid line) includes star formation in central and satellite galaxies, diffuse star formation in extended regions, and gravitational cooling. Their model without satellite galaxies is shown as dashed line, while their $\text{Ly}\alpha$ profiles arising from the central galaxy is marked as dotted lines. The model prediction given in Dijkstra & Kramer (2012) is shown in red. In both samples, the measurements closely match the theoretical expectations for $\text{Ly}\alpha$ photons arising from central star formation, leaving only a small room for possible contributions from other potential sources (see text for more discussion).

erature on the physical origin of the LAH phenomenon.

While there is no doubt that at least some $\text{Ly}\alpha$ emission

originates from the central star formation of the galaxy itself, $\text{Ly}\alpha$ photons emerging from the outer halo may still be contributed by multiple other sources: namely, star formation in satellite galaxies and diffuse gas around them; and gravitational cooling radiation from infalling gas. Their relative importance should sensitively depend on the total halo mass – which sets both the number of satellite galaxies and the rate of gas infall responsible for gravitational cooling radiation (Rosdahl & Blaizot 2012). However, different studies predict a wide range of $\text{Ly}\alpha$ halo luminosities resulting from gravitational cooling, even at a fixed halo mass (e.g. Faucher-Giguere et al. 2010). This results from the diverse physical conditions in the gas and complexities of modeling the radiative transfer. While the strength and spatial distribution of different ionizing sources are critical to determine LAH properties, their effectiveness are also related to the distribution and kinematics of gas and dust – which scatters and absorbs $\text{Ly}\alpha$ photons, respectively – in the interstellar and circumgalactic medium (Dijkstra & Kramer 2012, hereafter D12). Viewing angles may also play an important in the LAH appearance (Laursen & Sommer-Larsen 2007; Verhamme et al. 2012).

In this work, we compare our measurements with two recent models from D12 and Lake et al. (2015, hereafter L15). Together, these models bracket the two opposite ends of the possibilities.

The first model, proposed by D12, assumes that the central star formation as the sole power source of LAHs. $\text{Ly}\alpha$ photons are produced in the galaxy then propagate through an outflowing, cold, clumpy circumgalactic medium. The distribution and kinematics (i.e., outflow velocity field, HI column density, and degree of clumpiness as a function of galactocentric radius) of the CGM is set to reproduce reproduce the $z \approx 3$ halo structure derived using observations of QSO absorption lines as a function of impact parameter (Steidel et al. 2010).

Based on Monte Carlo simulations of radiative transfer for $\text{Ly}\alpha$ photons scattering through the CGM, D12 argued that significantly extended LAHs may be produced if the velocity field of gas clouds reaches a maximum at $r \sim 10$ kpc, beyond which clumps decelerate. Their best model produces a clearly extended LAH, but not as extended as that observed by S11.

In contrast to the D12 model, L15 takes into account all potential sources of $\text{Ly}\alpha$ production, including star formation from central and satellite galaxies, $\text{Ly}\alpha$ photons associated with diffuse UV background surrounding these galaxies, and gravitational cooling radiation. L15 simulated 9 LAEs at $z = 3.1$ using an adaptive mesh refinement hydrodynamical simulation of galaxy formation within a cosmological volume. This work re-simulates galaxies at higher resolution, reaching scales of ≈ 120 pc and mass resolution of $2 \times 10^7 M_\odot$. They model the $\text{Ly}\alpha$ emission from these haloes using the Monte Carlo radiative transfer code of (Zheng & Miralda-Escudé 2002), and create an average $\text{Ly}\alpha$ sur-

face brightness profile by combining the LAH models of individual galaxies. Each of the emergent $\text{Ly}\alpha$ photons is tagged according to its origin, which enables the authors to examine the relative importance of different components at different radii. L15 concluded that a significant fraction of their simulated LAHs must come from off-center star formation or gravitational cooling – contributes roughly equally – as their $\text{Ly}\alpha$ profile from the central SF falls steeply. The surface brightness profile from L15 gives an impressively good fit to the Momose et al. (2014) measurements except that it slightly overpredicts at $r > 10$ kpc. They further noted that the off-center SF may be suppressed because substantial SF in off-center locations would also lead to an extended UV continuum emission, which is not seen in the Momose et al. (2014) data. Exclusion of off-center SF brings their model to an even better agreement with the observational measurement.

The caveat of the D12 model is that it only considers photons arising from the central SF propagating through an outflowing medium, and ignores the possibility of an off-center SF and inflow of cold gas. On the other hand, L15 do not include the presence of an outflowing medium. The presence of ubiquitous outflows in high- z galaxies has been firmly established by observations (e.g. Steidel et al. 2010) and, as shown by D12, significantly impacts the emergent $\text{Ly}\alpha$ profiles. Apart from velocity fields, these two models differ in the relative distribution of gas and dust (clumpy vs smooth component) at radii relevant for the LAH phenomenon, although detailed discussions of these differences are beyond the scope of this paper.

Keeping in mind the differences between these models, we proceed to compare them with the measured LAH surface brightness profile. In Figure 10, we show the radial profile measurements for the full LAE sample (black) and that for point-like sources (gray) in the PCF and LAB field. The full L15 model, including central and off-center SF and gravitational cooling, is illustrated in solid blue line. Two variants of their model, by excluding the off-center SF or including only the central SF, are presented as dashed or dotted line, respectively. The D12 model is shown in red solid line. As we are mainly interested in comparing the large-scale behavior and not in evaluating the mean equivalent widths measured (assumed) in different samples (models), all curves are normalized at $r = 10$ kpc. It must be noted that we have convolved the model predictions to match the PSF broadening present in the data.

The D12 model predicts a remarkably good fit to the PCF measurement at $r = 0\text{--}30$ kpc, but slightly underpredicts the LAB profile, and declines with a shallower slope. The full model of L15 (solid blue line) overpredicts the surface brightness at $r > 10$ kpc and also falls more gradually than the data. Within the range $r = 10\text{--}30$ kpc, our PCF sample is best described by their ‘central SF only’ model while their model that in-

cludes gravitational cooling but without off-center SF (dashed line: labeled ‘without satellites’ in Figure 10) also lies well above our measurement. The LAB profile lies somewhere between their ‘central SF only’ model and ‘without satellites’ model although the slope is more similar to the former.

Our results indicate that the measured profiles are very close to that expected from Ly α photons arising from central star formation then scattered out to large radii, leaving only a small room for possible contributions from off-center SF (satellites and background diffuse SF) and gravitational cooling. It is conceivable that the deficit of the L15 ‘central-SF only’ model and our own measurements would be even smaller if they included an outflowing clumpy medium in their calculation, which in turn would result in broadening the central SF component.

At large galactocentric distances ($r > 10$ kpc), other mechanisms such as SF in satellites and gravitational cooling may contribute to the LAH phenomenon although it is difficult to speculate which process may dominate. In principle, a large contribution from satellite SF would result in similarly extended halos in the UV continuum image. Such a feature is not observed in our UV images although, similar to that discussed by Momose et al. (2016), robust detection of the feature requires both exceedingly low surface brightness sensitivities and a better control on sky subtraction precision. In particular, the latter is difficult to achieve as sky background estimation inherently includes these low-SB sources typically leading to over-subtraction, rendering the stacked image to appear more compact than the intrinsic size. Furthermore, a signal from off-center sources would be easily washed away by the median stacking method we adopted. Better constraints may come from ultra-deep NB observations which can resolve the morphologies of individual galaxies into compact or diffuse components.

One useful clue may come from the observed correlation between scalelengths and galaxies’ physical properties. One clear correlation that emerged from our analysis is that more extended LAHs are found around more UV-luminous galaxies. The trend may be explained in two different ways: first, the physical conditions (the kinematics and distribution of gas and dust) of more UV-luminous galaxies are more conducive to producing extended LAHs; and second, more UV-luminous galaxies – forming stars at higher rates – tend to be hosted by more massive halos (Giavalisco & Dickinson 2001; Ouchi et al. 2003; Lee et al. 2006; Hildebrandt et al. 2007) which are more likely to have a satellite galaxy (Hamana et al. 2004; Lee et al. 2009). In the latter scenario, it follows that galaxies in overdense environments are expected to have more pronounced Ly α halos in the average stack as, given everything else fixed, the likelihood of having a companion in proximity is enhanced by the factor that correlates with the overdensity param-

eter. If such a trend exists, it should have been observed in either of our samples as both fields contain highly significant galaxy overdensities. The complete lack of a trend between LAH size and overdensity parameters (as discussed in §5) suggests that satellite populations are not the dominant contributor to the LAH emission.

Interestingly, Duval et al. (2016) recently presented a detailed study of Mrk 1486, a local edge-on disk galaxy with a large LAH. As a source with one of the highest measured Ly α luminosities and equivalent widths in the LARS sample Hayes et al. (2013), Mrk 1486 also has physical properties (stellar mass, age, SFR, and dust content) similar to those of typical high-redshift LAEs (Hayes et al. 2014). Based on multiple line diagnostics, they concluded that Ly α photons are likely photoionized inside the disk then scattered in our direction by neutral gas in bipolar outflows. The physical picture presented by Duval et al. (2016) is qualitatively similar to ours and thus lends further support to our main conclusions.

7. SUMMARY

In this paper, we report robust detection of diffuse Ly α emission around high-redshift star-forming galaxies. Taking advantage of two large spectroscopic/photometric samples of galaxies at $z = 2.66$ and $z = 3.78$, we have examined how the LAH sizes correlate with the physical properties of galaxies, with rigorous tests of possible systematics in constructing stacked Ly α images and measuring LAH characteristics. Our main results are described as follows.

1. In our full samples and most of our subsamples, the stacked Ly α image is significantly more extended than the UV continuum image of the same galaxies and data point spread functions, unambiguously confirming the presence of diffuse Ly α emission. Typical sizes of LAHs in our samples are relatively modest at 4–8 kpc, in good agreement with recent measurements of individual galaxies (Wisotzki et al. 2016). Very large (> 15 kpc) LAHs similar to those reported by Steidel et al. (2011) are not detected.
2. We examine how LAH sizes – measured as an exponential scalelength – depend on galaxy properties: namely, UV luminosity, Ly α luminosity and equivalent widths, and local environment. In contrast to Matsuda et al. (2012), we find no correlation between LAH size and local environment – measured in galaxy overdensity – even though both of our samples contain significantly overdense structures which will likely evolve to massive galaxy clusters by the present epoch. The reason for the discrepancy is unclear. The strongest correlation is found with UV luminosity in our data. The same trend becomes even stronger when combined with other measurements in the literature.

We conclude that the physical processes that drive LAH sizes correlate strongly with galaxy's UV luminosity. The observed LAH trends with other galaxy parameters may be driven by the fact that they themselves weakly correlate with UV luminosity.

3. The measured scalelength – a characteristic scale with which an exponential function declines – should provide a reliable and robust metric to quantify an average LAH. Possible systematics inherent in the details of stacking procedure are examined by performing image stacking of an identical galaxy sample using a suite of methods bracketing various techniques employed in the existing literature. We compare the radial surface brightness profiles resulted from these methods, and find that while the overall amplitude of the profile is sensitive to the details of the adopted procedure, the overall shape is not.
4. We compare the LAH profiles measured in our data with recent theoretical predictions. A simple model in which Ly α photons originate from central star formation, then resonantly propagate outward in a clumpy outflowing medium, is in a reasonable agreement with our measurements. The implication is that other potential producers of Ly α photons, such as low-level star formation occurring in

off-center locations and radiative cooling of collisionally heated HI gas (gravitational cooling), may be at best minor contributors to the LAH phenomenon.

We thank the referee for a careful reading of the manuscript and for suggestions that helped improve this paper. This paper presents data obtained at the W. M. Keck Observatory (NASA proposal ID numbers 2014A-N116D and 2015A-N142D) and the Mayall 4m telescope of the Kitt Peak National Observatory (NOAO proposal ID numbers 2012A-0454, 2014A-0164 and 2014B-0626). We are grateful to the NASA Keck and NOAO Time Allocation Committees for granting us telescope time and to the staff of the W. M. Keck Observatory and the Kitt Peak National Observatory. Part of the observations reported here were obtained at the MMT Observatory, a joint facility of the University of Arizona and the Smithsonian Institution. We thank Y.-K. Chiang et al. for sharing the results of their protocluster studies to facilitate our overdensity calibration. We also thank Mark Dijkstra for providing insightful comments. AD's research is supported by the National Optical Astronomy Observatory (NOAO). NOAO is operated by the Association of Universities for Research in Astronomy (AURA), Inc. under a cooperative agreement with the National Science Foundation.

APPENDIX

A. CALCULATIONS OF Ly α LUMINOSITIES AND EQUIVALENT WIDTHS

Here, we briefly describe the procedure adopted to compute the rest-frame Ly α equivalent widths and line luminosities. Assuming a galaxy at redshift z whose continuum slope is described by a power law of $f_\lambda \propto \lambda^\beta$, the equivalent monochromatic flux density for a given passband containing both UV continuum and Ly α emission line can be expressed as follows:

$$f_{AB} \equiv 10^{-0.4(m_{AB}+48.6)} = \frac{F_{Ly\alpha}}{B} + f_{cont}Q \quad (A1)$$

where $F_{Ly\alpha}$ represents the integrated Ly α flux in units of $\text{erg s}^{-1} \text{cm}^{-2}$, and f_{cont} is the intrinsic specific continuum flux density near the Ly α line, in units of $\text{erg s}^{-1} \text{cm}^{-2} \text{Hz}^{-1}$.

B is the effective bandwidth measured in units of Hz, defined as:

$$B \equiv \frac{c \int \lambda^{-1} \mathcal{R}(\lambda) d\lambda}{\mathcal{R}(\lambda_0) \lambda_0}. \quad (A2)$$

Here, λ_0 is the Ly α wavelength in the observer frame and $\mathcal{R}(\lambda)$ is the system passband⁷.

⁷ The system bandpass here is measured in units of photon^{-1} , representing the system response function defined by the filter,

The dimensionless Q factor is defined as:

$$Q(z, \beta) \equiv \frac{\int e^{-\tau_{IGM}} (\lambda/\lambda_0)^{2+\beta} \lambda^{-1} \mathcal{R}(\lambda) d\lambda}{\int \lambda^{-1} \mathcal{R}(\lambda) d\lambda}, \quad (A3)$$

where τ_{IGM} denotes the effective optical depth of IGM as a function of wavelength, given by the prescription of Inoue et al. (2014). The IGM transmission prescription from Inoue et al. (2014) is based the updated statistics of the intervening absorption systems and comparable with the model from Meiksin (2006) above the Lyman continuum break. However, it generally predicts higher transmission than the commonly adopted model of Madau (1995). The Q factor represents two observational effects: the absorption by the IGM neutral hydrogen averaged over the bandpass, and the correction of different UV continuum slopes for the conversion between the AB magnitude and continuum specific flux density near Ly α . If the UV continuum slope is $\beta = -2$, the Q fac-

CCD quantum efficiency, and telescope/atmospheric transmission. We assume an airmass of 1.0 and adopt the transmission function of each filter from its respective website: *IA445*, <http://www.awa.tohoku.ac.jp/astro/filter.html>; *WRC4/BW/R/I*, <http://www.noao.edu/kpno/mosaic/filters>.

Table 5. Q and B Values for Our Datasets

NB-BB/ Redshift	β	Q_{NB}	B_{NB} Hz	Q_{BB}	B_{BB} Hz
$WRC4 - R$	-1.0	0.763	...	1.070	...
$z=3.790$	-1.5	0.763	3.726×10^{12}	1.006	1.284×10^{14}
	-2.0	0.762	...	0.948	...
$IA445 - B_W$	-1.0	0.808	...	0.795	...
$z=2.698$	-1.5	0.812	2.853×10^{13}	0.820	1.520×10^{14}
	-2.0	0.817	...	0.847	...

tor will be unity for a passband spanning the rest-frame wavelengths $\lambda > 1216\text{\AA}$.

When we have both narrow and broad bands (NB/BB) observations covering the $\text{Ly}\alpha$ line and adjacent UV continuum, the integrated line flux $F_{\text{Ly}\alpha}$ and the continuum specific flux density f_{cont} , can be derived and then expressed as:

$$F_{\text{Ly}\alpha} = \frac{B_{\text{BB}}B_{\text{NB}}}{Q_{\text{BB}}B_{\text{BB}} - Q_{\text{NB}}B_{\text{NB}}} \quad (\text{A4})$$

$$f_{\nu_0, \text{cont}} = \frac{B_{\text{BB}}f_{\text{AB}, \text{BB}} - B_{\text{NB}}f_{\text{AB}, \text{NB}}}{Q_{\text{BB}}B_{\text{BB}} - Q_{\text{NB}}B_{\text{NB}}} \quad (\text{A5})$$

The rest-frame equivalent width is then give as:

$$\text{EW}_0 = \frac{\text{EW}_{\text{obs}}}{1+z} = \frac{\lambda_0^2}{c} \frac{F_{\text{Ly}\alpha}}{(1+z)f_{\text{cont}}} \quad (\text{A6})$$

The values of Q and B depend the system bandpass, UV continuum slope and IGM absorption, with the last two of being model-dependent. The derived numerical values of the adopted NB/BB in our PCF and LAB datasets are listed in Table 5. By shifting the redshift of $\text{Ly}\alpha$ across the effective range selected by the NB filter and adjusting $\beta = -2 \sim -1$, we found that the relative error of continuum subtractions is below 10%.

B. COMPARISON OF STACKING METHODS

For constructing the $\text{Ly}\alpha$ surface brightness profile, previous studies employed different approaches to image masking, scaling/weighting and stacking. Most studies used a simple sigma-clipping approach, while we also experiment with *pixel-repaired* images as described in § 3.2 in this work. Images can be rescaled/weighted differently for the signal-to-noise optimization of the stacked image and outlier rejection. Finally, the image stacking can be performed by taking pixel-wise median or mean, typically on small-sized cutouts centered on each galaxy. If $\text{Ly}\alpha$ luminosities and LAH profiles vary significantly within a given sample, the light profile from mean stacks, compared with median stacks, may be biased towards sources with higher surface brightness. We

note that any low-level unmasked contaminants of each cutout can artificially enhance the signal, particularly for mean-combined stacks.

For the present work, we employ median image combination of pixel-repaired cutouts without further scaling and weighting. In comparison, S11 used straight mean image combination with masking, while Matsuda et al. (2012) adopted median image combination without masking. Momose et al. (2014) used two methods: one uses weighted mean image combination on sigma-clipped galaxy cutouts; the other uses median combination on scaled images. Feldmeier et al. (2013) first rescaled the NB images to a common flux level, then used sigma-clipped mean combination with weights proportional to the total NB flux of each galaxy.

In an effort to explore possible systematics inherent to different stacking techniques, we stack our full LAE sample using nine different stacking methods. These include: i) median combination with masking (*mkd_median*); ii) median combination of repaired images (*repair_median*), the method adopted in this work; iii) mean combination with masking (*mkd_mean*); iv) mean combination of repaired images (*repair_mean*); v) weighted mean combination with masking (*mkd_meanwt*); vi) weighted mean combination of repaired images (*repair_meanwt*); vii) median combination of rescaled images with masking (*mkd_mediansc*); viii) median combination of rescaled repaired images (*repair_mediansc*); and ix) straight median combination with no masking (*original_median*). For rescaling, we normalize each cutout by the $2''$ circular aperture flux to the median value of all galaxies in the sample.

The results of our test are illustrated in Figure 11 where we show the differential (top) and cumulative (bottom) radial profiles constructed using nine models together with the PSFs in both fields. All methods clearly detect extended emission compared with the PSF (dashed black line) in both profiles. The median stacks generally exhibit a slightly broader profile than the mean stacks, which is not unexpected for an intrinsically skewed distribution. However, the radial slope does not change significantly within the range which the exponential scalelengths are measured ($r \approx 2 - 5''$), resulting in most models having very similar scalelengths. More specifically, the exponential scalelength ranges from $r_s=5.4$ kpc (*repair_mean*) to 6.9 kpc (*original_median*) compared to our fiducial value, $r_s=5.8$ kpc (*repair_median*) for the PCF sample. No significant variation is found in the LAB sample. We also verify from this test that the pixel-repair technique returns a result consistent with simple masking of pixels.

Our test suggests that the *original_median* method leads to a slightly broader profile. The trend is most clearly illustrated from our test on the PCF sample (yellow line in Figure 11). We speculate that pixel-wise median combination may not be effective enough in re-

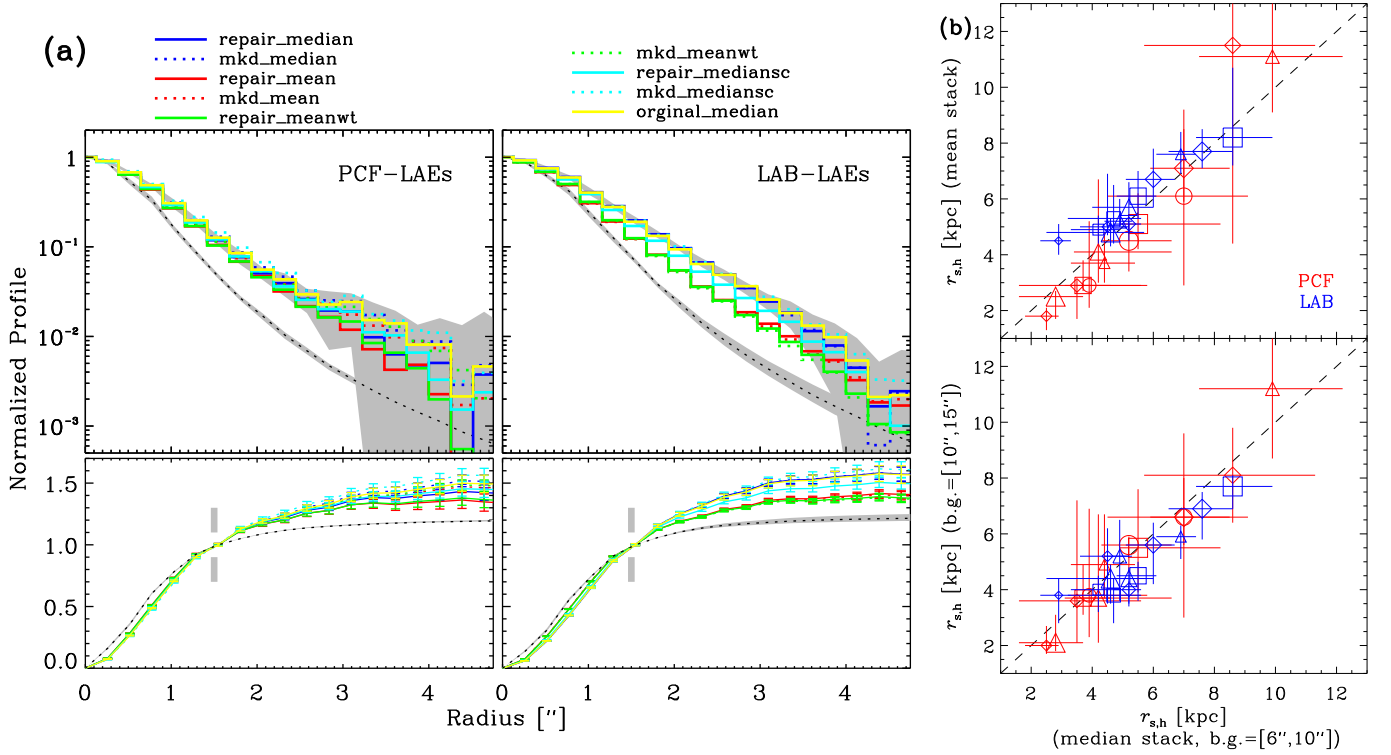


Figure 11. (a) Ly α radial profiles resulted from nine different stacking methods are compared. The full LAE sample is used for stacking in all methods. All differential profiles (top), including the PSF (dotted line), are normalized at center ($\theta = 0''$), while all cumulative profiles (bottom) are normalized at $\theta = 5''$. Estimated uncertainties of our fiducial model (repair_median stacking: blue solid line) are indicated as gray shades. We find that different methods generally return similar slopes in the radial profiles, but with a range of amplitudes. Scalelengths should provide a reliable metric for characterization of an average LAH. More discussion about the differences among different methods is given in text. (b) LAH scalelengths $r_{s,h}$ measurements using different image stacking and background estimation methods are shown for the PCF (red) and LAB (blue) subsamples. In both panels, these samples are defined according to their UV luminosities (square), Ly α luminosities (diamond), Ly α equivalent widths (triangle), and LAE overdensities (circle) as defined in Table 3 and Table 4, respectively. Symbol size increases as the median value of these quantities increases. In the top panel, the scalelengths measured from median- and mean-combined images are compared. In the bottom panel, the scalelengths are measured from median-combined image using different annular regions for sky background estimation. In both cases, we find that our scalelength measurements are robust against specific choices we made for deriving average radial profiles.

moving all contamination from a dataset of moderate size, which leads the stacked Ly α image to contain an enhanced level of flux out to very large radii. The scalelengths, $r_{s,h}$, from the two-component model are also robust against the details of how the image is created. In the left panel of Figure 11, we compare the values from the mean stack light profiles with those from the median stacking, for individual subsamples mentioned in §5. We find a reasonable agreement within the majority of subsamples. Our results presented in §5 do not change qualitatively if we adopted mean stacking instead.

The fluctuations in amplitude of measured radial profiles among different stacks are likely also linked to the precision of sky subtraction we are able to perform. As described in §3.2, a radial profile is measured from a “contamination-free zero-sky” image, which is con-

structed by estimating and subsequently subtracting sky background value from the stacked image itself. While this procedure does an excellent job ensuring that the pixels far from the central source are nearly background-free, the background value determined on the stacked image mildly fluctuates depending on the type of cutout images (i.e., *repaired*, *masked*, or *original*) and the choice of image combination (*mean* vs *median*).

Small uncertainties in sky background can alter the radial profile appearance especially in the low SNR regions. However, we find that the measured scalelengths are insensitive to specific choice adopted for sky background estimation. In the right panel of Figure 11, we show the $r_{s,h}$ values from our individual subsamples, using two different annular regions $r = [6'', 10'']$ and $r = [10'', 15'']$ to determine background levels. The former is adopted as our default method in this work. The

comparison shows a good consistency in $r_{s,h}$ despite very different choices of the annular regions adopted for sky subtraction.

We conclude that scalelength measurements offer a robust method to characterize radial profiles of diffuse Ly α emission than a comparison of the entire surface brightness profile shape. The latter is very sensitive to various systematics, namely, the manner in which image stacking and sky subtraction are performed, as well as the image PSF, which is further discussed below.

C. IMPACT OF PSF ON MEASUREMENTS OF SCALELENGTHS

Point spread functions with broad wings can significantly alter the observed shape of the Ly α emission (e.g., [Feldmeier et al. 2013](#)). Thus, the LAH exponential scalelengths from directly fitting Ly α radial profiles (Eq. 4) may be susceptible to the PSF effect. In this appendix, we use three toy models to illustrate the potential bias of this approach.

In our toy models, the Ly α emission from a typical start-forming galaxy consists of two components as described in Eq. 5: a halo component following an exponential profile with a scalelength $r_{s,h}$ of 3, 7, or 12 kpc in three models, respectively; and, a galaxy component modeled as exponentially declining with a scalelength of $r_{s,c} = 1.5$ kpc (a typical size of LAEs at our sample redshift). We define the halo-to-total Ly α fraction as:

$$X_{\text{Ly}\alpha} \equiv F_{\text{Ly}\alpha,\text{halo}} / (F_{\text{Ly}\alpha,\text{halo}} + F_{\text{Ly}\alpha,\text{galaxy}}) \quad (\text{C7})$$

where F denotes the total flux obtained by integrating the surface brightness profiles of the halo and galaxy component. In each of our models, we vary the halo-to-total Ly α fraction from $X_{\text{Ly}\alpha} = 20\%$ to 100% , with a ‘halo-only’ assumption corresponding to $X_{\text{Ly}\alpha} = 100\%$. Then we simulate the apparent Ly α radial profile by convolving intrinsic profiles from the toy models with the PSF measured from our LAB dataset. We evaluate the results from single-component exponential fitting to various simulated galaxy+halo profiles, and compare it with the intrinsic halo scalelengths (3, 7, or 12 kpc in three models, respectively).

In Figure 12(a), we present the simulated Ly α radial profiles with different halo-to-total Ly α fractions. In each panel, three halo models are shown in different colors. The halo-to-total Ly α fraction changes from 100% (top right), 75% (bottom left), to 25% (bottom right). In the ‘halo-only’ (or $X_{\text{Ly}\alpha} = 1$) model, the observed profile of the compact LAH model (3 kpc) closely follows the PSF, as the light profile of a compact source is essentially determined by the PSF. As for the 12 kpc LAH model, on the other hand, the profile is virtually unaltered by the PSF shape except within the central 5 kpc. Thus, if all Ly α emission originates from an LAH, the measured scalelengths should be relatively insensitive to a PSF falling off more steeply than the LAH. But if the

intrinsic LAH profile falls steeper than the PSF, a direct fitting of the apparent Ly α profile will lead to an overestimation of the LAH scalelength as the result only effectively characterizes the PSF shape. In more realistic scenarios of LAES, some compact Ly α emission may originate from the galaxy itself, which makes the intrinsic profile deviate from a purely exponential one. The outcome is that the observed Ly α profile can be significantly altered even for relatively large LAHs, as illustrated in the bottom panels of Figure 12. While compact LAH sources still resemble the PSF at large radii, even the profiles of large LAHs (up to 12 kpc here) will appear to steepen. The bottom-right panel of Figure 12 provide a simple explanation: the contribution from the compact Ly α emission, which resemble the PSF, becomes dominant in the integrated Ly α light profile. This leads to the underestimations of LAH sizes.

Figure 12(a) illustrates the potential bias of using the single-component exponential fit results to characterize LAH sizes. In Figure 12(b), we show the derive quantitative values of r_s from three toy models with varying halo-to-total Ly α fractions. Based on the toy models and the realistic PSF from our LAB sample, the single-component scalelength values from Eq. 5 can be only used to characterize LAH sizes when the halo appears to be broader than the actual PSF ($r_{s,h} \gtrsim 5$ kpc) and the compact Ly α component is not dominant ($X_{\text{Ly}\alpha} > 80\%$). The result also shows that even if all galaxies have identical intrinsic LAH sizes, varying $X_{\text{Ly}\alpha}$ parameter from 1 (LBG-like galaxies with no compact Ly α emission) to 0.2 (galaxies with prominent Ly α emission in centers) will decrease the estimated scalelength in a single-component exponential fitting.

This effect is indeed visible in several high UV/Ly α -luminosity subsamples (see Tables 3 and 4) and Figure 9, where the estimated scalelength from single-component fitting is lower. However, as the apparent light profile slope approach the slope in the PSF outer wings (an equivalent of scale-length ~ 5 kpc), the values of r_s overestimate the intrinsic LAH scalelengths.

Without the details of actual PSF in stacking images from previous studies, we are unable to quantify how significant this artificial effect could be. However, our simulation does suggest that one needs to exercise caution when interpreting the LAH scalengthes measured from different methods and how it the values changes with galaxy properties. For a simple scenario that all LAHs have the same scalelengths and the halo-to-total Ly α fraction is anti-correlated with the galaxy Ly α luminosity, we could expect an anti-correlation between the measured r_s and $L_{\text{Ly}\alpha}$ as we saw in [Momose et al. \(2016\)](#).

We note that the above bias would be less significant if the actual PSF can be approximated as a Gaussian function with less power in large radii. In the top left panel of Figure 12(a), we show a Gaussian profile with the same FWHM value as the actual homogenized PSF

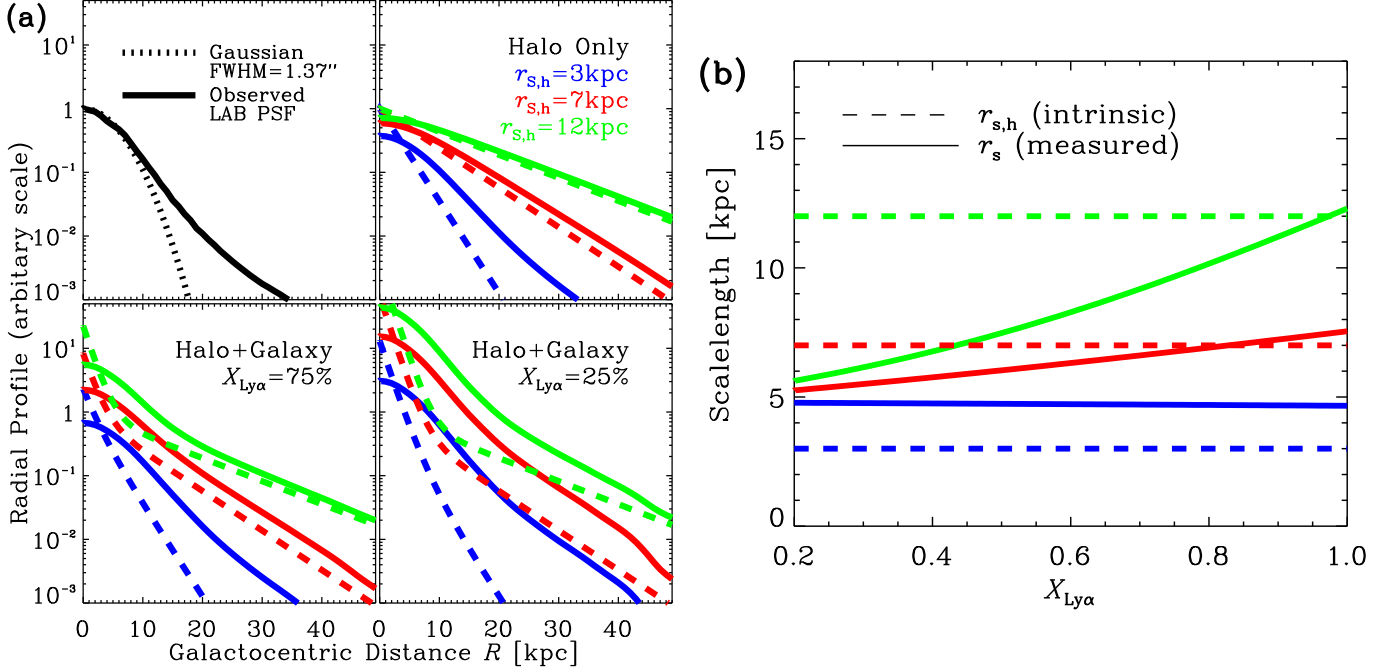


Figure 12. (a) PSF effects of measured $\text{Ly}\alpha$ profile are illustrated with three toy models. The surface brightness profile of an LAH is modeled as an exponentially declining function with scalelengths of 3 kpc (blue), 7 kpc (red), and 12 kpc (green); the SB profile of the central galaxy falls off with a scalelength of 1.5 kpc. The halo fraction, $X_{\text{Ly}\alpha}$, denotes the fraction of $\text{Ly}\alpha$ flux originating from the LAH component, and is assumed to be 100% (top right), 75% (bottom left), and 25% (bottom right). For each model, the intrinsic $\text{Ly}\alpha$ profile is a superposition of the two components (galaxy and halo), and is shown as a dashed line. The “observed” profile is created by convolving it with the actual homogenized PSF of our LAB sample, and is shown as a solid line. The PSF (top left, black line) – measured directly from our data – exhibits a broad wing, and as a result significantly alters the intrinsic profile by scattering centrally emitted photons to large radii. (b) We simulate $\text{Ly}\alpha$ profiles with different $X_{\text{Ly}\alpha}$ and convolve the intrinsic profiles with the realistic PSF present in the LAB field observation. Then we derive the single-component exponential scalelength r_s using the same procedure presented in §3.2, and present it as a function of $X_{\text{Ly}\alpha}$.

in the LAB field. Realistically, the resulting homogenized PSFs in both of our datasets are approximated by Moffat profiles with $\beta \approx 3.5$, which is typical in ground-based imaging (e.g. Dey & Valdes 2014). If the PSF homogenization of individual galaxy images is not de-

signed to precisely match the PSF shape before stacking and a simplified Gaussian convolving kernel is adopted, the effective PSF in stacking images will be poorly constrained beyond its FWHM. Comparisons of different subsamples in the LAH properties can be also precarious.

REFERENCES

- Bertin, E. 2011, *Astronomical Data Analysis Software and Systems XVIII*, 442, 435
- Bertin, E., & Arnouts, S. 1996, *A&AS*, 117, 393
- Bouwens, R. J., Illingworth, G. D., Franx, M., & Ford, H. 2007, *ApJ*, 670, 928
- Bouwens, R. J., Illingworth, G. D., Franx, M., et al. 2009, *ApJ*, 705, 936
- Carilli, C., & Rawlings, S. 2004, *New Astronomy Reviews*, 48, 979
- Charlot, S., & Fall, S. M. 1993, *ApJ*, 415, 580
- Chiang, Y.-K., Overzier, R., & Gebhardt, K. 2013, *ApJ*, 779, 127
- Ciardullo, R., Gronwall, C., Wolf, C., et al. 2012, *ApJ*, 744, 110
- Dey, A., Lee, K.-S., Reddy, N., et al. 2016, *ApJ*, 823, 11
- Dey, A., & Valdes, F. 2014, *PASP*, 126, 296
- Dey, A., Bian, C., Soifer, B. T., et al. 2005, *ApJ*, 629, 654
- Dijkstra, M., & Kramer, R. 2012, *MNRAS*, 424, 1672
- Duval, F., Östlin, G., Hayes, M., et al. 2016, *A&A*, 587, A77
- Faucher-Giguere, C.-A., Keres, D., Dijkstra, M., Hernquist, L., & Zaldarriaga, M. 2010, *ApJ*, 725, 633
- Feldmeier, J. J., Hagen, A., Ciardullo, R., et al. 2013, *ApJ*, 776, 75

- Gawiser, E., van Dokkum, P. G., Gronwall, C., et al. 2006, *ApJ*, 642, L13
- Giavalisco, M., & Dickinson, M. 2001, *ApJ*, 550, 177
- Giavalisco, M., Dickinson, M., Ferguson, H. C., et al. 2004, *ApJ*, 600, L103
- Guaity, L., Gawiser, E., Padilla, N., et al. 2010, *ApJ*, 714, 255
- Hamana, T., Ouchi, M., Shimasaku, K., Kayo, I., & Suto, Y. 2004, *MNRAS*, 347, 813
- Hayashino, T., Matsuda, Y., Tamura, H., et al. 2004, *ApJ*, 128, 2073
- Hayes, M. 2015, *Publ. Astron. Soc. Aust.*, 32, e027
- Hayes, M., Östlin, G., Schaerer, D., et al. 2013, *ApJ*, 765, L27
- Hayes, M., Östlin, G., Duval, F., et al. 2014, *ApJ*, 782, 6
- Hildebrandt, H., Pielorz, J., Erben, T., et al. 2007, *A&A*, 462, 865
- Hong, S., Dey, A., & Prescott, M. K. M. 2014, *PASP*, 126, 1048
- Inoue, A. K., Shimizu, I., Iwata, I., & Tanaka, M. 2014, *MNRAS*, 442, 1805
- Jannuzi, B. T., & Dey, A. 1999, *Astronomical Data Analysis Software and Systems XVIII*, 191, 111
- Jiang, L., Egami, E., Fan, X., et al. 2013, *ApJ*, 773, 153
- Jones, T. A., Ellis, R. S., Schenker, M. A., & Stark, D. P. 2013, *ApJ*, 779, 52
- Komatsu, E., Smith, K. M., Dunkley, J., et al. 2011, *The Astrophysical Journal Supplement*, 192, 18
- Koyama, Y., Kodama, T., Tadaki, K.-i., et al. 2013, *MNRAS*, 428, 1551
- Lake, E., Zheng, Z., Cen, R., et al. 2015, *ApJ*, 806, 46
- Lasker, B. M., Lattanzi, M. G., McLean, B. J., et al. 2008, *ApJ*, 136, 735
- Laursen, P., & Sommer-Larsen, J. 2007, *ApJ*, 657, L69
- Lee, K.-S., Dey, A., Cooper, M. C., Reddy, N., & Jannuzi, B. T. 2013, *ApJ*, 771, 25
- Lee, K.-S., Dey, A., Hong, S., et al. 2014, *ApJ*, 796, 126
- Lee, K.-S., Giavalisco, M., Conroy, C., et al. 2009, *ApJ*, 695, 368
- Lee, K.-S., Giavalisco, M., Gnedin, O. Y., et al. 2006, *ApJ*, 642, 63
- Lee, K.-S., Dey, A., Reddy, N., et al. 2011, *ApJ*, 733, 99
- Lemaux, B. C., Cucciati, O., Tasca, L. A. M., et al. 2014, *A&A*, 572, A41
- Madau, P. 1995, *ApJ*, 441, 18
- Matsuda, Y., Yamada, T., Hayashino, T., et al. 2004, *ApJ*, 128, 569
- . 2012, *MNRAS*, 425, 878
- Meiksin, A. 2006, *MNRAS*, 365, 807
- Momose, R., Ouchi, M., Nakajima, K., et al. 2014, *MNRAS*, 442, 110
- . 2016, *MNRAS*, 457, 2318
- Nilsson, K. K., Tapken, C., Möller, P., et al. 2009, *A&A*, 498, 13
- Oke, J. B., & Gunn, J. E. 1983, *ApJ*, 266, 713
- Ouchi, M., Shimasaku, K., Furusawa, H., et al. 2003, *ApJ*, 582, 60
- Ouchi, M., Shimasaku, K., Akiyama, M., et al. 2008, *The Astrophysical Journal Supplement Series*, 176, 301
- Petrosian, V. 1976, *ApJ*, 209, L1
- Prescott, M. K. M., Kashikawa, N., Dey, A., & Matsuda, Y. 2008, *ApJ*, 678, L77
- Prescott, M. K. M., Dey, A., Brodwin, M., et al. 2012, *ApJ*, 752, 86
- Rauch, M., Haehnelt, M., Bunker, A., et al. 2008, *ApJ*, 681, 856
- Rosdahl, J., & Blaizot, J. 2012, *MNRAS*, 423, 344
- Springel, V., White, S. D. M., Jenkins, A., et al. 2005, *Nature*, 435, 629
- Steidel, C. C., Adelberger, K. L., Giavalisco, M., Dickinson, M., & Pettini, M. 1999, *ApJ*, 519, 1
- Steidel, C. C., Adelberger, K. L., Shapley, A. E., et al. 2000, *ApJ*, 532, 170
- Steidel, C. C., Bogosavljević, M., Shapley, A. E., et al. 2011, *ApJ*, 736, 160
- Steidel, C. C., Erb, D. K., Shapley, A. E., et al. 2010, *ApJ*, 717, 289
- Tumlinson, J., Thom, C., Werk, J. K., et al. 2013, *ApJ*, 777, 59
- Verhamme, A., Dubois, Y., Blaizot, J., et al. 2012, *A&A*, 546, 111
- Williams, C. C., Giavalisco, M., Lee, B., et al. 2015, *ApJ*, 800, 21
- Wisotzki, L., Bacon, R., Blaizot, J., et al. 2016, *A&A*, 587, A98
- Zheng, Z., Cen, R., Weinberg, D., Trac, H., & Miralda-Escudé, J. 2011, *ApJ*, 739, 62
- Zheng, Z., & Miralda-Escudé, J. 2002, *ApJ*, 578, 33